Dissertation for Doctoral Degree at Chiba University

Understanding of Molecular Interaction on Interfaces for Carbon Dioxide Removal and Ion Storage.

August 2019

Chiba University

Graduate School of Science

Department of Chemistry

Md Sharif Khan

Contents

Chapter 1

Introduction:

The rapid increasing concentration of atmospheric carbon dioxide (CO_2) due to the anthropogenic emissions is one of the greatest environmental concern of the present time. Access level of CO_2 present in the atmosphere can make major climate changes and global warming as it can cause greenhouse effect by absorbing and emitting radiation within thermal infrared region. Since the industrial revolution, CO_2 concentration has greatly increased and surpassed 400 ppm in 2013[1]. Around 86% of the world's primary energy sources are currently based on fossil fuels (coal, petroleum, and natural gas), and these CO_2 emissions are projected to continue to increase in the foreseeable future due to economic growth and industrial development. It is predicted that this increasing atmospheric CO_2 concentration will not be altered within the next several decades, because fossil fuels will still be the dominant energy source, particularly in developing nations. In 2004 out of 77% of the total anthropogenic greenhouse gas emitted close to 60% was attributed to large stationary emission sources, such as power plants, gas processing industries, refineries, chemical and petrochemical industries, iron and steel industries, and cement industries. Three approaches are envisaged for CO_2 capture from fossil fuel based power plants: pre-combustion, post-combustion, and oxy-combustion[2]. Pre-combustion capture is applicable to integrated gasification combined cycle plants, while oxy-combustion and post-combustion could be applied to conventional coal- or gas-fired power plants. The capturing of the CO_2 from atmosphere after post-combustion is one of the most useful way to reduce the concentration of CO_2 in atmosphere. However, before considering a material as a CO_2 sorbent we have to focus on the criteria those can make a material useful CO_2 sorbent.

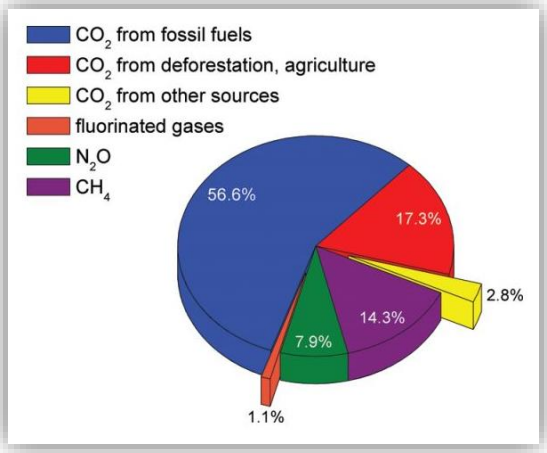

Figure 1: Sources of CO_2 in atmosphere according to percentile

Criteria for Selecting CO_2 Sorbent Material. Sorbent selection is a complex problem. The sorbent materials must satisfy some important criteria to be both economical and operational for CO_2 capture from flue gas. These criteria are listed in this section[3-4].

• **CO_2 Adsorption Capacity:** The performance of the sorbent materials mostly justified by their equilibrium adsorption capacity. The amount of the adsorption should be in a good ratio with the sorbent used thus can be cost effective. However, sometimes the high adsorption capacity for CO_2 can reduces sorbent quantity and process equipment size. In practice, working capacity, defined for a short adsorption time, is preferred to be used in place of equilibrium capacity.

• **Selectivity:** The selectivity for CO_2 adsorption by a sorbent can be defined by the ratio of the CO_2 capacity to that of different component or gas like N_2 at a given flue gas composition, can directly involve on the purity of CO_2 captured. The purity of CO_2 has impacts on transportation and sequestration have high dependency on the purity of CO_2 and, therefore, plays an important role in CO_2 sequestration economics. The flue gas streams produced from the fossil-fuel fired power plants contain N_2 and O_2 combine with CO_2. The materials those exhibit high CO_2 selectivity over these other bulk gas components can be considered as a good sorbent. In case of solid sorbents, it is equally

important to show high capacity for CO_2 even though flue gas contain significant amounts of water vapor.

• **Kinetics of Adsorption/Desorption:** At a given operating conditions the materials should have fast adsorption/desorption kinetics for CO_2.The cycle time of a fixed-bed adsorption system can be controlled by the kinetics of adsorption and desorption. a sharp CO_2 breakthrough curve can be found for fast kinetics in which effluent CO_2 concentration changes are measured with the change of time, while an inflated breakthrough curve can be seen for slow kinetics. Both of these influence on the amount of required sorbent. In case of the presence of functional group in a solid sorbent the overall kinetics of CO_2 adsorption is dominated by the intrinsic reaction kinetics of CO_2 with the functional group, further the mass transfer or diffusion capability of the gas phase through the sorbent structures. The porous support structures with functional group solid sorbents also can be tailored, to increase the diffusion capability. The faster if an adsorbent can adsorb CO_2 faster than can be desorbed faster, the less of it will be needed to capture a given volume of flue gas.

• **Mechanical Stability of Sorbent:** Microstructure and morphological stability must be demonstrated by the selected sorbent. alongside during the multi cycling between the absorption and regeneration steps the sorbent has to be retained the CO_2 capture capacity. In order to maintain high kinetics Microstructure and morphological stability of tailored regenerable sorbents in multicycle operation is critical. The differentiation of the sorbent particles should be regardless to the operating conditions, such as high volumetric flow rate of flue gas, vibration, and temperature. Therefore, to minimize the sorbent reproducibility rate and keep the CO_2 adsorption process cost-effective the adequate mechanical strength of sorbent particles is crucial.

• **Chemical Stability of the Sorbent:** Solid CO_2 capture sorbents especially, the sorbents contain amine functional group should be stable in an oxidizing environment of the flue gas and have high resistant to contaminants of common flue gas. In most of the cases gaseous contaminants such as SO_x, NO_x as well as heavy metals will also

require removal from flue gas, since they have significant negative impact on the CO_2 adsorption capacity of the sorbent materials.

• **Regeneration of Sorbents:** The heat of adsorption should be considerable low, which is a measure of the energy required for regeneration. In case of physisorption heats of adsorption are usually in the range of 25 to 50 kJ mol^{-1}. Whereas for chemisorption is it 60 to 90 kJ mol^{-1}. Furthermore, in the powerplant flue gas environment, the sorbent should be regenerable through a suitable pathway during the repeated adsorption desorption cycles as well as maintaining efficient CO_2 sorption capacity. The cost of capture can be reduced due to the ease regeneration of the CO_2 sorbent.

• **Sorbent Costs:** This is one of the most important characteristics for an ideal sorbent. A baseline dragged by researcher of approximately $10/kg for sorbents in their sensitivity analysis for cost effective performance. According to them, a cost of $5/kg sorbent results in a very good and a cost of $15/kg sorbent should consider as expensive. Therefore, to be more economical, the cost of the CO_2 capture sorbent should be in the range of approximately $10/kg for an ideal adsorbent the above-mentioned attributes are essential. It is difficult for a single adsorbent to have all of these attributes. However, those will be considered as useful adsorbents that can effectively and economically capture CO_2 from flue gas.

In the past decades research on developing efficient adsorbents with a substantial capacity, good stability and recyclability has grown rapidly. Nanoporous materials have been considered as good candidates for this protesting task due to their high surface area, highly porous structure and high stability. In recent developments, plenty of nanoporous materials such as zeolites, metal organic frameworks (MOFs), mesoporous silicas, carbon nanotubes and organic cage frameworks etc. have been included in the CCS technology.

Zeolites are aluminosilicate minerals with ordered, nanoporous structures. Zeolites have been extensively used in industry as adsorbents and catalysts, because of their high surface area, specific porous structures and availability in large quantities. Commonly, the pore size of zeolites is ranging from 0.3 to 1.2 nm, however, since the size of a CO_2

molecule is 0.54 nm in length and 0.31 nm in dimeter, therefore, zeolites with pore size of 0.4 to 0.5 nm can be high affinitive to CO_2. Due to the ion exchange with cations of alkali metals provides the basicity in zeolites, which is considered as a leading property for the selective CO_2 adsorption over other gases like N_2 and H_2O. the cation size of the zeolites affects their distribution in the pores, while their polarity also affects the polarization of adsorbed CO_2[5]. Furthermore, Si/Al ratio also have a great influence on adsorption capacity of the zeolites, higher cation exchange can be found for lower Si/Al ratio which provide more available cation for interacting with CO_2 hence higher adsorption capacity. Moreover, in case of pore size, smaller pores lead to show a higher affinity towards CO_2 rather than N_2 and O_2 as ambient pressure which means high adsorption capacity as well as the rate of adsorption[6]. Zeolites have already been widely used in many industrial processes. However, zeolites can be deactivated in presence of moisture which lead to a significant reduction in CO_2 adsorption capacity, therefore, application of zeolites in CO_2 capture from power plant flue gas has not been as successful.

Metal Organic Frameworks (MOFs) have ordered structures constructed with transition metal ions interconnected with organic struts those are commonly molecules with aromatic groups terminated with the functional groups capable of coordinating to metal ions mainly carboxylic acid group or aromatic ring incorporated with nitrogen atoms. Most of the MOFs show nanoscale porosity, resulting a large internal surface area with a variety of window sizes. By varying the size and nature of the components used in the synthesis it is possible to tune the MOFs structural properties for a particular task, which is one of the major advantage of MOFs over other adsorbent materials. For the purpose of post-combustion CO_2 capture and ideal material would exhibit a high selectivity to CO_2 over N_2 as well as good volumetric and gravimetric uptake of CO_2 with these requirements several MOFs performed well, with the isomorphous CPO-27 series showing very high levels of uptake with good selectivity[7]. The ability for selective CO_2 adsorption in a gaseous mixture determine whether a MOF system is a suitable candidate for use in CCS as well as having a scalable synthesis and ability to adsorb or desorb CO_2 in a rapid time scale. Due to the high adsorption capacity, selectivity, recyclability and unique structural tunability, MOFs have been regarded as

some of the best candidate for the ultimate task of CO_2 capture. However, only small quantities of active MOFs materials are possible to synthesize, which is considered as a major limitation to use MOFs for industrial purpose. Furthermore, sine the MOFs are built with toxic transition metals as ligands, these materials may cause severe environmental problems upon deposal.

Mesoporous silicas have high surface are and high pore volume, hence it has been used as a sorbent for many species including gases, organic pollutants and biomolecules. Unlike zeolites and MOFs the larger pore size of mesoporous silicas implies that, without modification the intrinsic interaction between the guest molecules and the adsorbent is weaker specifically at low pressure. Salinization methods have been introduced for the synthesis of organic-inorganic hybrid mesoporous silica, using functionalized alkoxy silanees with grafting amine group onto the mesoporous silica surface. These basic amine groups can provide strong attraction towards CO_2 and the adsorption capacity of amine functionalized mesoporous silica varies with the conditions of measurement and the preparation methods. In contrast with zeolite, CO_2 adsorption capacity increase when functionalized mesoporous silicas introduced with water because of the formation of protonated ammonium ions and carbonates. By the removal of deactivation due to water has added benefit that amine functionalized mesoporous silica could be used in a temperature swing adsorption CCS system. In amine functionalized mesoporous silica sample CO_2 adsorption capacity should be proportional to the amine content at a ratio of $N:CO_2 = 2:1$, therefore if the amine groups are to be diamine or triamine groups then the adsorption capacity should be doubled or even tripled. However, scientist still attempted to fill these mesopores with polyamines to maximize the CO_2 adsorption capacity. Mesoporous silicas can be prepared at room temperature and pressure with scaling up the synthesis. Moreover, in case of industrial use large scale production is possible. In term of environmental influence, functionalized mesoporous silicas do not rely on toxic metals or ligands for the adsorption of CO_2, although the environmental impact of amine groups is still unknown.

Due to the hydrophobic nature and high surface area nanoporous carbon materials including carbons and carbon fibres have considered as adsorbents for CO_2 adsorption. Moreover, most of the carbon materials are relatively cheap to manufacture and light in weight. Between all of carbon materials carbon nanotubes (CNT) both single walled and multi walled have been extensively studied as an adsorbent for carbon dioxide. However, theoretical investigation of the adsorption of CO_2 using carbon nanotubes is mostly take place rather than experimental investigation because carbon nanotube preparation is bit expensive than other nanoporous carbon materials. On the other hand, a type of nanoporous carbon materials can be prepared from mesoporous silica templates, which seems to similar kinds of characters like carbon nanotube and been used for CO_2 adsorption and separation. Although scaling up production of these ordered carbon nanomaterials at a possible kilogram scale production has been reported[8] the more suitable candidate among this group of carbon materials for CO_2 adsorption is still microporous activated carbon. This is mainly because their production cost and scale of preparation are much more realistic for large scale applications. Nevertheless, these carbon-based materials are neutral, be more selective for CO_2 they need further chemical modification. Amination of activated carbon in one popular method for modifying the surface in order to enhance selectivity toward CO_2 due to the improved surface basicity.

In the past few years plenty of porous organic nanomaterials have caught the attention. Similar to MOFs systems, Organic Cage Framework (OCF) materials contain repeated units of cage like ordered structures are formed from purely organic without any metal component. Specific size of the cage can lead the separation CO_2 from other gases as well as the presence of the amine in the cage provide a large number of active sites for CO_2. Covalent organic frameworks (COFs) is another class of porous organic nanomaterials are formed from the frameworks of the molecules which are able to react with one another vis strong covalent bonds. Super molecular organic frameworks (SOFs) is another class of pure type organic framework has been reported to show interesting reversible gas adsorption properties[9]. Presence of the non-covalent interactions such as hydrogen bonds and π-π stacking interactions stabilized the crystalline porous SOF system. Despite their considerable potential, research in OCF, COF, and SOF systems is still relatively in its infancy compared to the much more

widely studied systems of zeolites, MOFs and supported amines. Therefore, additional effort is still required to make any of these porous organic frameworks a realistic candidate for CO_2 capture on an industrial scale.

As mentioned above, around the world fossil fuels are the most widely used energy source and which act as a major source of the CO_2 in the atmosphere, alternative cleaner, efficient and sustainable energy sources are essentially important as well as the technology associated with this kind of energy conversion and storage. Researcher have been proposed various renewable energy sourced such as wind, solar and wave. However, among various energy storage technologies, electrical double layer capacitances (EDLCs) have been attracted the attention for large-scale energy storage system due to its high energy conversion efficiency, flexibility and comfortable maintenance. This energy storage device store energy by accumulation of the change on the electrode surface as electric double layer[10]. The EDLCs have potential application in order to achieve the increasing demand for energy storage technologies like renewable energy, smart grid management and electrical vehicles[10-13]. An EDLC can be built with two electrodes, an electrolyte, a separator that protect from the short circuit of the two electrodes. In order to having maximum charge density, the specific surface area of an EDLC electrode should be higher. The good electrode materials have to maintain some criterion such as maintain higher energy and power density, cost-effective, nontoxic and safe, and the easier production. In the industry level to the date most commonly used electrode materials are activated carbon.

Regarding electrolytes, there are three different kind of electrolytes can be used in the EDLC.

Aqueous electrolytes: Aqueous electrolytes can provide a significantly higher ionic concentration and lower resistance. Due to the smaller ionic radius of the aqueous electrolytes and the relative higher ionic concentration, EDLC consist with aqueous electrolytes may provide relatively higher capacitance and higher power density. Unlike other electrolytes, aqueous electrolytes can be prepared and use without maintaining strict control of the preparing processes and conditions. However, aqueous electrolytes have relatively small potential windows up to 1.2 V. This is one of the major limitations for using aqueous electrolytes since the potential windows is very low compare with

other electrolyte candidates such as organic electrolytes and ionic liquids. Due to the narrow windows potential of aqueous electrolytes they are limited to further improvement of their power and energy density.

Organic electrolytes: Organic electrolytes have been considered as a potential candidate for EDLC, since they can provide a higher potential window around 3.56 V. This is one of the major reasons to use organic electrolytes over aqueous electrolytes sometimes. Among of the different organic electrolytes available, propylene carbonate and acetonitrile have been used mostly. However, acetonitrile has severe toxicity and bed impact on environment, although acetonitrile can dissolve large amount of salt rather than other organic electrolytes. While propylene carbonate has higher conductivity and wide potential window as well as it can operate at wide range of temperature. Apart these two electrolytes researchers have been suggested many more organic electrolytes those can be used for EDLC. However, the performance of the organic electrolytes always can be limited due to the impurity and poor operating conditions. For instance, organic electrolytes potential window can be significantly reduced due to the presence of water above 3-5 ppm

Room Temperature Ionic Liquids: In presence of heat or might be at room temperature the salt can be melted in order to counterbalance the salt lattice energy, such kind of systems called molten salts or ionic liquids. Ionic liquids can be kept in liquid form at desire temperature. Ionic liquids posses' properties like low vapor pressure, high thermal and chemical stability with high potential window around 4.5 V, and high conductivity, these properties make them a suitable electrolyte candidate for EDLC. Furthermore, ionic liquids are solvent free at liquid form, thus no solvation shell can be involved during the charge discharge process. Which could be helpful to identify the actual ionic size. The chemical and physical properties of the ionic liquids mainly depend on the type of cation and anion. A wide number of ionic liquids have been suggested by the different researcher around the world to use for EDLC. However, ionic liquids have high toxic impact on the environment. Furthermore, the performance can be interrupted due to the presence of the water, as ionic liquids are highly additive with the water vapour.

In the higher power demand applications for power buffering, power saving and energy recovery, recently EDLCs are being used potentially[13-16]. One of the major potential future application of the EDLCs is to use in the transport industry, for example use in the personal vehicles, buses, trucks and trains, in order to provide energy rapidly for acceleration[11, 17] Furthermore, EDLCs can be potentially use in the portable and flexible electronic devices, memory backup and energy harvesting[18-19]

References:

1. Monastersky, R., Global Carbon Dioxode Levels near Worrisome Milestone. *Nature* **2013**, *497*, 13-14.

2. Herzog, H. J., Peer Reviewed: What Future for Carbon Capture and Sequestration? *Environmental Science & Technology* **2001**, *35*, 148A-153A.

3. Yong, Z.; Mata, V.; Rodrigues, A. r. E., Adsorption of Carbon Dioxide at High Temperature—a Review. *Separation and Purification Technology* **2002**, *26*, 195-205.

4. Sayari, A.; Belmabkhout, Y.; Serna-Guerrero, R., Flue Gas Treatment Via Co2 Adsorption. *Chemical Engineering Journal* **2011**, *171*, 760-774.

5. Hernández-Huesca, R.; Díaz, L.; Aguilar-Armenta, G., Adsorption Equilibria and Kinetics of Co2, Ch4 and N2 in Natural Zeolites. *Separation and Purification Technology* **1999**, *15*, 163-173.

6. Dunne, J. A.; Rao, M.; Sircar, S.; Gorte, R. J.; Myers, A. L., Calorimetric Heats of Adsorption and Adsorption Isotherms. 2. O2, N2, Ar, Co2, Ch4, C2h6, and Sf6 on Nax, H-Zsm-5, and Na-Zsm-5 Zeolites. *Langmuir* **1996**, *12*, 5896-5904.

7. Mason, J. A.; Sumida, K.; Herm, Z. R.; Krishna, R.; Long, J. R., Evaluating Metal–Organic Frameworks for Post-Combustion Carbon Dioxide Capture Via Temperature Swing Adsorption. *Energy & Environmental Science* **2011**, *4*, 3030-3040.

8. Wang, J.; Xue, C.; Lv, Y.; Zhang, F.; Tu, B.; Zhao, D., Kilogram-Scale Synthesis of Ordered Mesoporous Carbons and Their Electrochemical Performance. *Carbon* **2011**, *49*, 4580-4588.

9. Yang, W., et al., Exceptional Thermal Stability in a Supramolecular Organic Framework: Porosity and Gas Storage. *Journal of the American Chemical Society* **2010**, *132*, 14457-14469.

10. Gogotsi, Y.; Simon, P., True Performance Metrics in Electrochemical Energy Storage. *Science* **2011**, *334*, 917-918.

11. Faggioli, E.; Rena, P.; Danel, V.; Andrieu, X.; Mallant, R.; Kahlen, H., Supercapacitors for the Energy Management of Electric Vehicles. *Journal of Power Sources* **1999**, *84*, 261-269.

12. Dunn, B.; Kamath, H.; Tarascon, J.-M., Electrical Energy Storage for the Grid: A Battery of Choices. *Science* **2011**, *334*, 928-935.

13. Simon, P.; Gogotsi, Y., Materials for Electrochemical Capacitors. *Nature Materials* **2008**, *7*, 845.

14. Kötz, R.; Carlen, M., Principles and Applications of Electrochemical Capacitors. *Electrochimica Acta* **2000**, *45*, 2483-2498.

15. Largeot, C.; Portet, C.; Chmiola, J.; Taberna, P.-L.; Gogotsi, Y.; Simon, P., Relation between the Ion Size and Pore Size for an Electric Double-Layer Capacitor. *Journal of the American Chemical Society* **2008**, *130*, 2730-2731.

16. Frackowiak, E., Carbon Materials for Supercapacitor Application. *Physical Chemistry Chemical Physics* **2007**, *9*, 1774-1785.

17. Pan, H.; Li, J.; Feng, Y., Carbon Nanotubes for Supercapacitor. *Nanoscale Research Letters* **2010**, *5*, 654.

18. Merlet, C.; Rotenberg, B.; Madden, P. A.; Taberna, P.-L.; Simon, P.; Gogotsi, Y.; Salanne, M., On the Molecular Origin of Supercapacitance in Nanoporous Carbon Electrodes. *Nature Materials* **2012**, *11*, 306.

19. El-Kady, M. F.; Kaner, R. B., Scalable Fabrication of High-Power Graphene Micro-Supercapacitors for Flexible and on-Chip Energy Storage. *Nature Communications* **2013**, *4*, 1475.

Chapter 2

Methodology

2.1 Adsorption

Adsorption phenomenon is equilibrium phenomenon between the interfaces such as solid-liquid, solid-gas, and liquid-liquid. The model of adsorption between a solid-gas phase is shown in Figure 1. In the case of the solid-gas phase, the adsorbed layer density near the solid surface is higher than the bulk density and gradually decreases to some as the bulk gas density when the distance from the solid surface becomes far. This phenomenon is widely used for the study on the state of the surface and nanostructure analysis in academic and for the material storage, separation, and catalysis in industry. The most common terms use in the adsorption field can be define as follows[1]; **Adsorption:** Enrichment of one or more components in an interfacial layer; **Adsorbate:** Substance in the adsorbed state; **Adsorptive:** Adsorbable substance in the fluid phase; **Adsorbent:** Solid material on which adsorption occurs.

Figure 1: The solid-gas phase model of adsorption

2.2 Physical Adsorption and Chemical Adsorption:

The adsorption phenomena are distinguished in physical and chemical adsorption. Physical adsorption is caused by the interaction which is mainly the dispersion force

between the surface and molecules and forms the multilayer because the interaction force works for a long distance around several nm. On the other hand, chemical adsorption is caused by the charge transfer interaction or chemical bond generation between the surface and molecules and confined to only a monolayer. Therefore, the properties of physical and chemical adsorption are different as shown in Table 2.1.

Table2.1: Comparison of physical and chemical adsorption

	Physical Adsorption	Chemical Adsorption
Adsorption amount	> Monolayer Capacity	< Monolayer
Adsorption Rate	Quick	Slow
Heat of Adsorption	<100 KJ / mol	> 100 kJ / mol
Specific Interaction	None	Dominant
Reversibility	Dominant	None

2.3 Adsorption Isotherm:

The measurement of an adsorption isotherm is carried out by mainly two methods, the gravimetric method and the volumetric method[2-4]. All of the adsorption isotherms were measured in this thesis by using volumetric method.

The adsorption amount is obtained from the pressure change using the ideal gas equation or the can der Waals equation. The volumetric method apparatus is composed of the vacuum part, the gas reservoir, the sample cell, and the pressure measuring parts shown in the Figure 2. Although the apparatus of volumetric method is simple compared with that of gravimetric method, it is difficult of obtain the accurate

adsorption amount because it is necessary to keep the temperature at constant and to measure the accurate dead and sample volumes. The ideal gas or van der Waals equations are not used for the calculation of the adsorption amount due to the error in the high-pressure adsorption. The most disadvantage of this method is that the volumetric method tends to increase the error every measured point.

Regarding the measurement of adsorption isotherms[5], the adsorption amount, n, on the solid surface depends on the measuring pressure, temperature, natures of the fluid and the solid. Thus, the adsorption amount can be expressed as

$$n = f\ (P, T, fluid, solid) \qquad (2.1)$$

In general, the adsorption measurement carried out a function of pressure at constant temperature T, and then the equation can simply to

$$n\ =\ f\ (P)_{T,gas,solid} \qquad (2.2)$$

This relation is called the adsorption isotherm. When the temperature is below the critical temperature, the equation is given by using saturate vapor pressure P_0

$$n\ =\ f\ (\frac{P}{P_0})_{T,gas,solid} \qquad (2.3)$$

Where $\frac{P}{P_0}$ is relative pressure.

The phenomenon in which the adsorbate adsorbs on the interface is termed the adsorption. On the contrary, the phenomenon in which the adsorbate leaves from the interface is termed the desorption. If the adsorption amounts of the adsorption process do not coincide with that of the desorption process, this phenomenon is called the

hysteresis. The adsorption amount is always smaller than the desorption amount in the hysteresis region. There was a group of six different physisorption isotherms recommended by IUPAC in the 1985[6]. However, last few decease researchers have been identified several new types of isotherms and demonstrated the relevancy of those isotherms with pore structures[7]. Therefore, in the 2015 the classification has been updated as shown in the Figure 2[8]

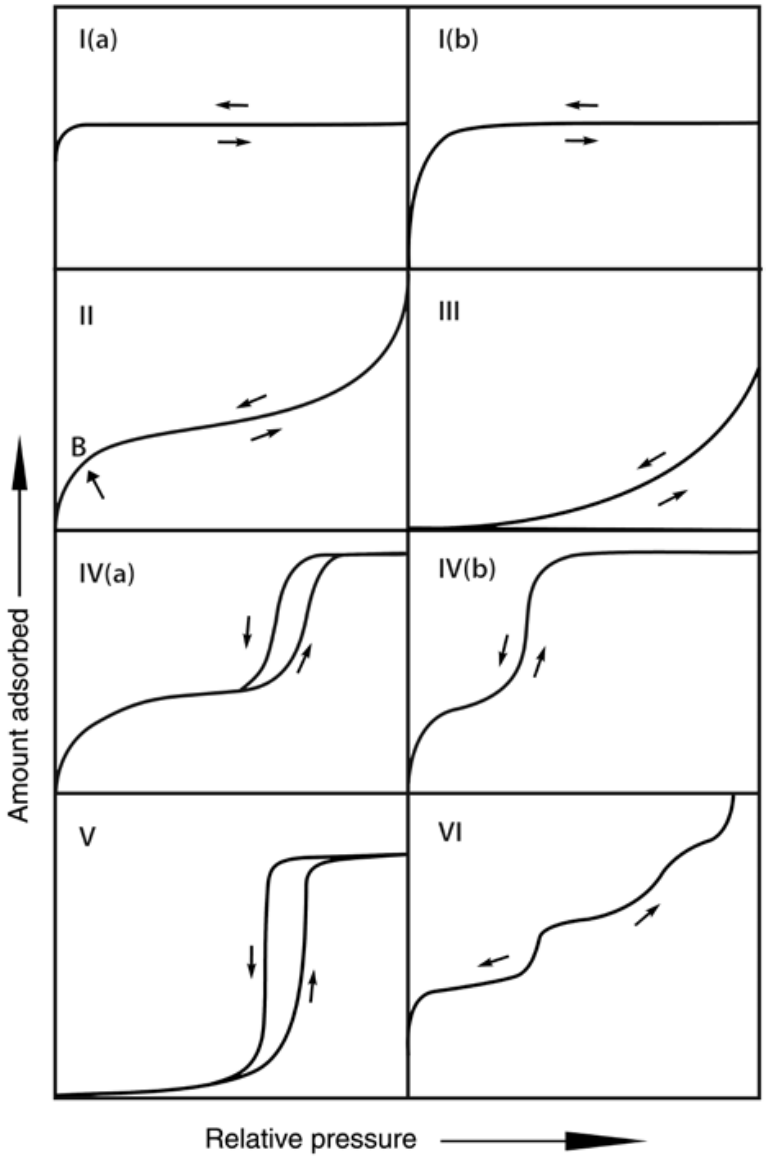

Figure 2: Classification of physisorption isotherms recommended by IUPAC.

The microporous materials such as activated carbons, molecular sieve zeolites and certain porous oxide etc. with comparative small external surfaces can give Type 1 isotherms. Type 1 isotherms, which is called Langmuir isotherm, is concave to the relative pressure (P / P_0) axis and the adsorption amount approaches a limiting value as P / P_0 approaches. The microporous materials mainly having narrow micropores width of less than 1 nm demonstrate Type 1(a) isotherms, whereas materials with boarder range pore size distributions including wider micropores and narrow mesopores less than 2.5 nm.

Type II isotherms is obtained with a nonporous or microporous adsorbent. This type of isotherms represents multilayer adsorption. It is explained by Brunauer, Enammet, and Teller. Therefore, Type II is called BET type. The Knee of the Type II isotherm, called point B as shown in the Figure 3, is usually considered to represent the completion of a monolayer and beginning of the formation of the multilayer.

Type III isotherms are convex to the P / P_0 axis over its entire range. Type III isotherms is caused by stronger adsorbate-adsorbate than adsorbate-adsorbent interaction. This isotherm is shown in the adsorption of water on nonporous carbon materials.

Type IV isotherms is related to capillary condensation in mesoporous adsorbents such as oxide gels, industrial adsorbents and mesoporous molecular sieves. The adsorbent - adsorptive interactions and the interaction between the molecules in the condensed state are directly related with the nature of adsorption in mesoporous materials. The capillary condensation which accompanied by hysteresis has been considered as Type IVa isotherm. Pore width when exceeds a certain critical width incorporate with adsorption system and temperature produce this type of isotherms[9-10]. Completely reversible Type

IVb isotherm observed when the materials having mesopores of smaller width. Alongside, Type IVb adsorption isotherm can also be seen for conical and cylindrical mesopores with closed tapered end.

Type V isotherm is also related to capillary condensation in mesopores and observed with hysteresis loop. Type V is similar to Type III except for existing of mesopores. This isotherm is shown in the adsorption of water on microporous carbon materials.

Type VI isotherms is called the stepwise isotherm. This isotherm associated with layer by layer adsorption on a uniform non-porous solid. For example, this type isotherm is observed in the adsorption on a uniform non-porous solid. For example, this type of isotherms is observed in the adsorption of Kr on the perfect graphite such as High Orientated Pyrolytic Graphite (HOPG).

In the case of supercritical gas adsorption, as the capillary condensation do not occur in the supercritical state and the adsorbate-adsorbate interaction is weaker than adsorbate-adsorbent interaction due to the molecules having high energy, Type I or Type II isotherm can be observed[7]. However, the raw data of the adsorption isotherm differ from each isotherm because of the adsorption amount.

The Brunauer-Emmett-Teller (BET)[11] method is widely used for the determination of the surface area of the solid materials from adsorption isotherms. The BET theory is based on the Langmuir Kinetic theory. Although Langmuir theory assumes that the adsorption occurs only monolayer, the BET theory assumes that the adsorption occurs multilayer on the surface. Furthermore, it assumes that the first adsorption layer

interacts with solid surface and the adsorbed molecules of higher layer interact with only the adsorbed molecules. The BET equation is expressed as

$$\frac{n}{n_m} = \frac{C_x}{(1-x)(1-x+C_x)} \qquad (2.4)$$

Here, n_m is the monolayer capacity, C is the constant value related to the energy of adsorption in the first adsorbed layer, and x is the relative pressure (P/P_0). The equation 2.4 can change to 2.5

$$\frac{x}{n(1-x)} = \frac{C-1}{n_m C}x + \frac{1}{n_m C} \qquad (2.5)$$

The BET equation requires a linear plot of $\frac{x}{n(1-x)}$ vs x in the relative pressure range of 0.05 to 0.3. This linear region is shifted to lower relative pressure of 0.01 to 0.10 for micropores materials. The n_m and C are obtained form the slop and intercept of the plot. The specific surface area, S, can be determined from n_m value. The specific surface area is calculated by next equation.

$$S = \frac{n_m N a_m}{100\ M} \qquad (2.6)$$

Here the unit of n_m is mg/g, N is the Avogadro constant, M is the molecular weight of adsorbate, and a_m is the average area occupied by a molecule of adsorbate. a_m is 0.162 $nm^2$for N_2 adsorption at 77 K. In other gases, a_m is obtained from the literature[12-14]. Although the n_m value is also obtained from the Langmuire equation, this n_m is not applicable to porous material containing both micropores and meso and/or macropores.

2.4 Molecular Dynamics (MD) Simulation:

Molecular Dynamics (MD) simulation is technique for computing the equilibrium and transport properties of a classical many body system. In this contest the word classical means that the nuclear motion of the constituent particles obeys the laws of classical mechanics. This an excellent approximation for a wide range of materials. only when we consider the translational or rotational motion of light atoms or molecules or vibrational motion with a frequency should we worry about quantum effect. Of course, our discussion of this vast subject is necessarily incomplete. Other aspects of the MD simulation techniques can be found in the different literatures[15-17].

MD simulations are in many respects very similar to real experiments. When we perform a real experiment, we prepare a sample of the material that we wish to study. We connect this sample to a measuring instruments and we measure the property of interest during a certain time interval. If our measurements are subject to statistical noise, then the longer we average the more accurate our measurement becomes. In a MD simulation, we follow exactly the same approach. First, we prepare a sample: we select a model system consisting of N particles and we solve Newtons equations of motion for this system until the properties of the system no longer change with time which means we equilibrate the system. After equilibration, we perform the actual measurement. In fact, some of the most common mistakes that can be made when performing a computer experiment are very similar to the mistakes that can be made in real experiments for example, the sample is not prepared correctly, the measurement is too short, the system undergoes an irreversible change during the experiment, or we do not measure what we think. To measure an observable quantity in a MD simulation we

must first of all be able to express this observable as a function of the position and momenta of the particles in the system. For instance, a convenient definition of the temperature in a many-body system makes use of the equipartition of energy over all degrees of freedom that enter quadratically in the Hamiltonian of the system. In particular for the average kinetics energy per degree of freedom we have,

$$\frac{1}{2}mv_{\alpha}^{2} = \frac{1}{2}k_{B}T \qquad (2.6)$$

In a simulation er use this equation as an operational definition of the temperature. In practice, we would measure the total kinetic energy of the system and divide this by the number of degrees of freedom N_f (= 3N – 3 for a system of N particles with fixed total momentum). As the total kinetic energy of a system fluctuates so does the instantaneous temperature:

$$\mathrm{T(t)} = \sum_{t=1}^{N} \frac{m_i v_i^2(t)}{k_B N_f} \qquad (2.7)$$

The relative fluctuations in the temperature will be of order $\frac{1}{\sqrt{N_f}}$ as N_f is typically on the order of 10^2 - 10^3, the statistical fluctuations in the temperature, one should average over many fluctuations.

2.4.1 Force Calculation:

One of the most time-consuming part of almost all MD simulations: the calculation of the force acting on every particle. If we consider a model system with pairwise additive interactions, we have to consider the contribution to the force on particle *i* due to all its neighbours. If we consider only the interaction between a particle and the nearest image

of another particle, this implies that for a system of N particles we must evaluate N × (N-1)/2 pair distances. This implies that, if we use no tricks, the time needed for the evaluation of the forces scales as N^2. There exist efficient techniques to speed up the evaluation of both short-range and long-range forces in such a way that computing time scales as N, rather than N^2. If a given pair of particles is close enough to interact, we must compute the force between these particles is close enough to interact we much compute the force between these particles and the contribution to the potential energy.

During the MD simulations, interaction between particles mostly calculate as Lennard-Jones (LJ) potential and columbic pairwise interaction with a cutoff value. LJ potential calculates by the equation 2.8, where U(r) is the energy between two particles at a distance of r, σ indicate the size of the particle and the well depth ϵ characterizes the attraction between the particles. On the other hand, equation 2.9 help to calculate the columbic pairwise interaction between the particles. Where, C is an energy conversion constant, changes of the two atoms considered by q_i and q_j. dielectric constant is used in the formula with symbol μ

$$\mathbf{U(r)} = \mathbf{4\epsilon}\left[\left(\frac{\boldsymbol{\sigma}}{\mathbf{r}}\right)^{\mathbf{12}} - \left(\frac{\boldsymbol{\sigma}}{\mathbf{r}}\right)^{\mathbf{6}}\right] \qquad (2.8)$$

$$\mathbf{E} = \frac{\boldsymbol{C_{q_i q_j}}}{\boldsymbol{\mu r}} \qquad (2.9)$$

2.4.2 Equation of Motion:

It is obvious that a good MD simulation program requires a good algorithm to integrate Newtons equations of motion. In this sense, the choice of algorithm is crucial. However, although it is easy to recognize a bad algorithm, it is not immediately obvious what criterial a good algorithm should satisfy. Let us look at the different points to consider.

Although, at first sight, speed seems important it is usually not very relevant because the fraction of time spent on integrating the equations of motion is small, at least for atomic and simple molecular systems.

Accuracy for large time steps is more important, because the longer the time step that we can use the fewer evaluations of the forces are needed per unit of simulation time. Hence, this would suggest that is advantageous to use a sophisticated algorithm that allows use of a long-time step.

Algorithms that allow the use of a large time step achieve that by strong information on increasingly higher order derivatives of the particle coordinates. As a consequence, they tend to require more memory storage. For one considers very large systems, the amount of memory needed to store these derivatives is small compared to the total amount available even on a normal workstation.

Energy conservation is an important criterion, but actually we should distinguish two kinds of energy conservation, namely short time and long time. The sophisticated higher order algorithms tend to have very good energy conservation for shot times. However, they often have the undesirable feature that the overall energy drifts for long times. In contrast, varlet-style algorithms tend to have only moderate short-term energy conservation but little long-term drift.

It would seem to be most important to have an algorithm that accurately predicts the trajectory of all particles for both short and long times. In fact, no such algorithm exists. For essentially all systems that we study by MD simulations, we are in the regime where the trajectory of the system through phase space. Depends sensitively on the

initial conditions. This means that two trajectories that are initially very close will diverge exponentially as time progresses. We can consider the integration error caused by the algorithm as the source for the initial small difference between the "true" trajectory of the system and the trajectory generated in our simulation. We should expect that any integration error, no matter how small, will always cause our simulated trajectory to diverge exponentially from the true trajectory compatible with the same initial conditions. This so-called Lyapunov instability would seem to be a devastating blow to the whole idea of MD simulations but we have good reasons to assume that even this problem need not be serious.

Clearly, this statement requires some clarification. First of all, one should realize that the aim of MD simulation is not to predict precisely what will happen to a system that has been prepared in a precisely known initial condition: we are always interested in statistical predictions. We wish to predict the average behaviour of a system that was prepared in an initial state about which we know something but by no means everything. In this respect, MD simulations differ fundamentally from numerical schemes for predicting the trajectory of stellated through space: in the latter case, we really wish to predict the true trajectory. We cannot afford to launch an ensemble of satellites and make statistical predictions about their destination. However, in MD simulations, statistical predictions are good enough. Still, this would not justify the use of inaccurate trajectories unless the trajectories obtained numerically, in some sense, are close to true trajectories. This layer statement is generally believed to be true, although, to our knowledge, it has not been proven for any class of systems that is of interest for MD simulations. However, considerable numerical evidence, suggests that there exist so-

called shadow orbits. A shadow orbit is a true trajectory of a many body system that closely follows the numerical trajectory for a time that is long compared to the time it takes the Lyapunov instability to develop. Hence the result of our simulation is presentative of a true trajectory in phase space, even though we cannot tell a priori which. Surprisingly, it appears that shadow orbits are better behaved for systems in which small differences in the initial conditions lead to an exponential divergence of trajectories that for the seemingly simpler systems that show no such divergence[18]. Despite this reassuring evidence[19], it should be emphasized that it is just evidence and not proof. Hence, our trust in MD simulations as a tool to study the time evolution of many body systems is based largely on belief. To conclude this discussion, let us say that there is clearly still a corpse in the closet. We believe this corpse will not haunt us, and we quickly close to closet. The more details can be found the literatures[19-21]

Newton's equation of motion is time reversible and so should be our algorithms. In fact, many algorithms are not time reversible. That is, future and past phase space coordinates do not play a symmetric role in such algorithms. As a consequence, if one were to reverse the momenta of all particles ate given instant, the system would not trace back its trajectory in phase space, even if the simulation would be carried out with infinite numerical precision. Only in the limit of an infinitely short time step will such algorithms become reversible. However, what is more important many seemingly reasonable algorithms differ in another crucial respect from Hamilton's equation of motion: rue Hamiltonian dynamics leaves the magnitude of any volume element in phase space unchanged, many numerical schemes, in particular those that are not time reversible do not reproduce this area preserving property. This may sound like a very

esoteric objection to an algorithm, but it is not. Again, without attempting to achieve a rigorous formulation of the problem, let us simply note that all trajectories that correspond to a particular energy E are contained in a volume Ωin phase space. If we let

Hamilton's equation of motion act on all points in this volume, then we end up with exactly the same volume. However, a non-area preserving algorithm will map the volume Ωon another volume Ω`. After sufficiently long times, we expect that the non-

area preserving algorithm will have greatly expanded the volume of our system in phase space. This is not compatible with energy conservation. Hence, it is plausible that non-reversible algorithms will have serious long-term energy drift problems. Reversible, area-preserving algorithms will not change the magnitude of the volume in phase space. This property is not sufficient to guarantee the absence of long-term energy, but it is at least compatible with it. It is possible to check whether an algorithm is area preserving by computing the Jacobian associated with the transformation of old to new phase space coordinates.

Finally, it should be noted that even when we integrate a time reversible algorithm, we shall find that the numerical implementation is hardly ever truly time reversible. This is so, because we work on a computer with finite machine prevision using floating point arithmetic that results in rounding errors.

2.4.3 MD simulations by LAMMPS:

In this thesis, simulations were performed using the November 4, 2016 release of LAMMPS "Large-scale Atomic/Molecular Massively Parallel Simulator" – a classical

MD program from Sandia National Laboratories. It implements the MD simulation algorithms and is capable of running on single processor or in parallel. Two main inputs are required in LAMMPS: (1) An input data file containing information about atom types, initial coordinated, bonds, angles, dihedral and improper quadruplets, and (2) and input script. A LAMMPS input script is typically sub-divided into 4 parts:

1. Initialization: Set parameters that need to be defined before atoms can be read from the input data file.
2. Atom Definition: Atom types, initial coordinated and molecular topology information such as bonds, angles, dihedral and improper quadruples are read from an input file. Alternatively, atoms can be directly created on a lattice by specifying relevant rules, but this is not performed in this thesis.
3. Settings: Once atoms and molecular topology are defined many types of settings can be specified. They include force field coefficients, simulation parameters, fixes such as boundary conditions and integration methods), peripheral computations and output options.
4. Run simulation: Perform energy minimization and run the simulation.

References:

1. F. Rouqurol, J. R., and K. Sing, Adsorption by Powder and Porous Solids: Principles, Methodology and Applications. *Academic press, San Diego* **1999**.

2. Hammett, L. P., The Effect of Structure Upon the Reactions of Organic Compounds. Benzene Derivatives. *Journal of the American Chemical Society* **1937**, *59*, 96-103.

3. McBain, J. W.; Bakr, A. M., A New Sorption Balance1. *Journal of the American Chemical Society* **1926**, *48*, 690-695.

4. Kaneko, K.; Shimizu, K.; Suzuki, T., Intrapore Field-Dependent Micropore Filling of Supercritical N2 in Slit-Shaped Micropores. *The Journal of Chemical Physics* **1992**, *97*, 8705-8711.

5. Steele, W. A., The Physical Interaction of Gases with Crystalline Solids: I. Gas-Solid Energies and Properties of Isolated Adsorbed Atoms. *Surface Science* **1973**, *36*, 317-352.

6. Sing, K. S. W., Reporting Physisorption Data for Gas/Solid Systems with Special Reference to the Determination of Surface Area and Porosity (Recommendations 1984). In *Pure and Applied Chemistry*, 1985; Vol. 57, p 603.

7. Murata, K.; Kaneko, K., Nano-Range Interfacial Layer Upon High-Pressure Adsorption of Supercritical Gases. *Chemical Physics Letters* **2000**, *321*, 342-348.

8. Thommes, M.; Kaneko, K.; Neimark Alexander, V.; Olivier James, P.; Rodriguez-Reinoso, F.; Rouquerol, J.; Sing Kenneth, S. W., Physisorption of Gases, with Special Reference to the Evaluation of Surface Area and Pore Size Distribution (Iupac Technical Report). In *Pure and Applied Chemistry*, 2015; Vol. 87, p 1051.

9. Thommes, M.; Cychosz, K. A., Physical Adsorption Characterization of Nanoporous Materials: Progress and Challenges. *Adsorption* **2014**, *20*, 233-250.

10. Monson, P. A., Understanding Adsorption/Desorption Hysteresis for Fluids in Mesoporous Materials Using Simple Molecular Models and Classical Density Functional Theory. *Microporous and Mesoporous Materials* **2012**, *160*, 47-66.

11. Brunauer, S.; Emmett, P. H.; Teller, E., Adsorption of Gases in Multimolecular Layers. *Journal of the American Chemical Society* **1938**, *60*, 309-319.

12. Steele, W. A., Concerning a Theory of Multilayer Adsorption, with Particular Reference to Adsorbed Helium. *The Journal of Chemical Physics* **1956**, *25*, 819-823.

13. McClellan, A. L.; Harnsberger, H. F., Cross-Sectional Areas of Molecules Adsorbed on Solid Surfaces. *Journal of Colloid and Interface Science* **1967**, *23*, 577-599.

14. Ismail, I. M. K., Oxidation of Rayon Fabrics in Atomic and Molecular Oxygen. *Carbon* **1990**, *28*, 401-409.

15. Tildesly, M. P. A. a. D. J., Computer Simulation of Liquids. *Clarendon Press, Oxford* **1987**.

16. Haile, J. M., Molecular Dynamics Simulations: Elementary Methods *Willey, New York* **1992**

17. Pontikis, M. M. a. V., Proceedings of Nato Asi on Computer Simulation in Materials Science. *Kluwer, Dordrecht* **1991**.

18. Tremain, G. D. Q. a. S., On the Reliability of Gravitational N-Body Integration *Mon. Not. R. Astrom. Soc.* **1992**, *259*, 505-518.

19. Gillilan, R. E.; Wilson, K. R., Shadowing, Rare Events, and Rubber Bands. A Variational Verlet Algorithm for Molecular Dynamics. *The Journal of Chemical Physics* **1992**, *97*, 1757-1772.

20. Cizeau, P.; Bouchaud, J. P., Theory of L\'Evy Matrices. *Physical Review E* **1994**, *50*, 1810-1822.

21. Vesely, F. J., Computational Pysics, an Intruduction. . *Plenum, New York* **1994**.

Chapter 3

High CO_2 Sensitivity and Reversibility on Nitrogen-Containing Polymer by Remarkable CO_2 Adsorption on Nitrogen Sites

3.1. Introduction

Global warming and climate change are the major challenge in the twenty first century, while accelerating level of atmospheric carbon dioxide (CO_2) is considered the major reason.[1-2] The concentration of CO_2 in the atmosphere has significantly increased, reaching 400 ppm in 2013.[3] It is essential to maintain the atmospheric concentration of CO_2 below 450 ppm to reduce the temperature increase to 2.48–2.88 K. In order to attain this objective, CO_2 emissions must be reduced by 30%–60% by 2050.[4-5] Major energy sources such as coal, petroleum and natural gas are based on fossil fuels make up approximately 86% of all energy sources, and it will be difficult to restrict the atmospheric CO_2 concentration in the upcoming decades as fossil fuels remain the most useful energy source, especially in developing countries.[6] Carbon capture and storage as well as carbon capture and utilization have been explored worldwide, in order to decrease the CO_2 concentration in the atmosphere. Adsorption and membrane separation have been considered a suitable technology for CO_2 capture because of the low energy requirements.[7] Porous materials such as porous carbon,[8-13]metal organic frameworks,[14-15] zeolites,[16-19] porous organic polymers,[20] nanoporous dipeptide-based materials,[21] amine-modified silicas,[22-23] and others[24-28] have been available as efficient materials for CO_2 removal. However, porous carbons have limited considering CO_2/N_2 selectivity from atmospheric gas mixture porous carbons have poor performance and zeolites are highly hydrophilic in nature thus inefficient at capturing CO_2 from flue gases with water

vapor.[6] Polymer-based adsorbent materials with high thermal and hydrothermal stability have recently attracted great interest owing to low density, large surface area, and high porosity.[29-33]

Introduction of heteroatoms like nitrogen into the porous polymers and carbons can significantly accelerate CO_2 adsorption capability and selectivity.[34-36] According to Chen *et al.* microporous polycarbazole shows high CO_2 capture amount of 4.8 mmol g^{-1} at 273 K.[37] Nitrogen rich porous polymers shows more than 4.28 mmol g^{-1} synthesized by Hug *et al*.[38] Nitrogen site rich porous organic polymer benzimidazole produced high CO_2 capability of 5.3 mmol g^{-1} at 273 K and 0.1 MPa.[39-40] Carbon spheres containing mesopores and nitrogen sites synthesized by Li *et al.* provide CO_2 capture capability of 2.9 mmol g^{-1} at 0.1 MPa and 298 K.[41] in spite of the significant usefulness of the using a nitrogen-rich adsorbent materials for CO_2 capture, the mechanism of domination by nitrogen sites for CO_2 capture not necessarily clear. The significant increase of CO_2 capture capability of nitrogen-containing surfaces is facilitated by the interactions between acidic CO_2 molecules and basic nitrogen groups.[42] Carbon surface containing nitrogen atoms can generate hydrogen bonding with CO_2, which can increase the CO_2 adsorption amount reported by Xing *et al.*[43] In contrary, Sevilla *et al.* reported the smaller impact of nitrogen functionalities on CO_2 capture.[44] On the other hand, from MD simulation Kumar *et al*. suggested that micropores plays significant role for capturing CO_2, while micropores with nitrogen atoms rarely influenced the CO_2 capture amount.[45] Therefore, a study that compare experiments and simulations is essential to address these controversies.

In this chapter we reported a in details experimental and molecular dynamics (MD) simulations study on CO_2 capturing and sensing performances of organic polymers as a function of temperature (243, 273, and 303 K). Two different kind of organic polymers were synthesized on carbon nanotubes, one is containing nitrogen atoms in structure (named as N-polymer) to elucidate the effect of nitrogen atoms on CO_2 adsorption and other one without nitrogen atoms in structure (named as C-polymer) for comparison. Synthesis procedure for the organic polymers are reported elsewhere.[46]

3.2. Experimental and Simulation Procedures

In order to synthesize nitrogen atom atoms doped N-polymer, 28 mg of divinyl-1,10-phenathroline (DVP) dissolved in tetrahydrofuran (THF) was impregnated on 10 mg of a single-walled carbon nanotube (SWCNT) support.[47] After impregnation at reduced pressure condition the samples were dried at 333 K for 1 h and then sealed in ampoule tubes under the same pressure condition. In order to restrain the polymerization of DVP beforehand vaporization the tubes were placed in a furnace that was initially heated at either 673 K or 773 K, after that kept at mentioned temperatures for 1 h. After this treatment remaining precursors have to be removed, to do this the samples were transferred to new glass tubes and again heated at 413 K for 1 h. Similarly, to synthesize polymer without nitrogen atoms i.e. C-polymer, 127.2 mg of divinyl-1,10-phenanthrene (DVPA) dissolved in THF was impregnated on 45.8 mg of a SWCNT support using a nascent wetness impregnation method. Rest of the procedure was the similar to the procedure used for N-polymer. All of the adsorption isotherms were measured using a volumetric apparatus (Autosorb-1, Quantachrome Instrument,

Florida, USA) beforehand vacuum evacuation was performed at 423 K for more than 2 h. the specific surface area was calculated from the nitrogen adsorption isotherms those were measured at 77 K using The BET equation.[48] Different temperatures such as 243 K, 273 K, and 303 K were considered for measuring CO_2 adsorption isotherms.

In case of gas sensing measurements, 1 mg of N-polymer and C-polymer was immersed in 2 mL of isopropyl alcohol and used ultrasonication for 1 h to disperse the polymers. Tiny amounts of both polymer solutions were deposited onto a 10-μm gap indium tin oxide electrode. Before starting CO_2 gas sensing measurement, the polymer deposited electrodes were heated at 363 K for 5 min in a nitrogen atmosphere. At temperature 297 K and electrical potential 5V a four-probe electrical resistivities of the polymers were measured. First the polymers were introduced to 10^4 ppm CO_2 gas at a time duration of 60s and then nitrogen gas was introduced to refresh.

Large-scale Atomic/Molecular Massively Parallel Simulator (LAMMPS) molecular dynamics code was used to perform MD simulations. The initial configuration of the simulation systems were prepared by using Packmol and moltemplete.[49-50] In the all-atom structure of N-polymer consist 142 atoms and C-polymer consist 152 atoms (Figure 1a). Both the polymers build with head-to-tail connection pattern using the exist vinyl groups. In case of N-polymer four monomer units were used, while five monomer units were used for of C-polymer. In order to calculate the partial charge distribution throughout the polymer structures we used the semi-empirical AM1-BBC method; this is a widely used method, which can provide more precise partial charge distributions in the polymer structures. the standard 12-6 Lennard–Jones (LJ) potential was used to model the interactions between the particles.

Further, coulombic pairwise interaction was also considered with a cut-off length of 10.0 Å. In case of graphene, the lattice structure was assumed as honeycomb and the change for carbon atoms was considered zero. The potential parameters were σ_G = 3.40 Å and ε_G = 0.556 kcal/mol while the C-C distance was 1.42 Å.[51] TraPPE potential was used to construct the CO_2 model.[52] According to this model, the CO_2 molecule was considered as a linear triatomic molecule in which every atom consist charge at the center.. The LJ parameters for the C and O atoms from the TraPPE force field were given by σ_C = 2.8 Å and ε_C = 0.0537 kcal/mol and σ_O = 3.05 Å and ε_O = 0.157 kcal/mol, respectively. Furthermore, to construct the quadrupole moment of the CO_2 molecules in the model carbon atoms consist point charge of +0.70e at the center of mass and each oxygen atoms consist a charge of −0.35e. The GAFF force field was used for the both N-polymer and C-polymer in order to construct the all atom potential. This force field has a great consistency with the AMBER force field and contain all of the available parameters.[53-54] The Lorentz – Berthelot mixing rules were adopted for all Lennard – Jones interactions between different kinds of molecules.

During the adsorption of CO_2 to omit the effect of one side on the other in all simulation systems two-layer graphene was used. The 8 nm × 8 nm two graphene consisted 5016 atoms and the distance between the two layers of graphene around 3.35 Å. This two layer graphene was positioned in the center of a $9 \times 9 \times 22$ nm^3 unit cell. 20 C-polymer and 25 N-polymer molecules were adsorbed on each side of the two-layer graphene. For the polymer adsorption on the graphene surfaces, MD simulations were conducted for 1 ns at 150 K temperature. In order of abstain the vibration and dislocation of the graphene atoms all the graphene was rigid during the simulations. In

the three-dimensional periodic boundary condition 200–3000 CO_2 molecules were randomly placed for different systems. Different temperatures such as 243 K, 273 K and 303 K were considered and the Nosé–Hoover algorithm was used to maintain the temperature. Equilibration of the systems was attained after 2 ns simulation. CO_2 molecules those were within the distance of 2 nm of the graphene surface considered as adsorbed, while others in the bulk.

3.3. Results and Discussion

Figure 1a illustrated the skeleton structure of the N-polymer and C-polymer. The polymers generated from the phenanthrene forms unit structure and the N-polymer has zigzag structure while C-polymer has linear structres.[55] Electrostatic potential distribution through the structure of N-polymer and C-polymer were depicted in figure 1b after optimization of structure using a semi-empirical calculation (AM1) with bond charge correction, which was parameterized to reproduce the HF/6-31G* RESP charge. Ununiform electrostatic charge distribution throughout the structure can be seen in N-polymer, while C-polymer was almost neutral. Furthermore, N atomic sites of N-polymer contained relatively higher negative partial charges and the edges of the ring contained the positive charges. In case of the C-polymer, ring edges contained small negative charges while the vinyl part was neutral. Therefore, compared to the N-polymer, weaker adsorbed-adsorbent interaction can be seen in C-polymer. Nitrogen adsorption isotherms at temperature 77 K depicted in the figure 1c were used to calculate the specific surface area. According to the IUPAC classification the shape of the adsorption isotherms showed in Figure 1c were almost similar to type II, however small hysteresis can be seen, proposing the behavior like type IVa .[56] These results

indicate that N-polymer and C-polymer both had almost non-porous surfaces with tiny amount of mesopores. Owing to the presence of cylindrical nanopores the carbon nanotubes nitrogen adsorption isotherm was typical. The Brunauer–Emmett–Teller (BET) analysis method was used to calculate the specific surface area. The BET surface areas of N-polymer were 30 m^2 g^{-1}, while it was 25 m^2 g^{-1} for C-polymer. By considering the declining of the BET surface area of carbon nanotubes after polymer fabrication, the layer number of the fabricated polymers were assumed. According to the assumption the N-polymer formed 25 layers while C-polymer form 40 layers and 0.29 and 0.40 nm^2 are the molecular area of the unit molecules, and different polymer only reflecting different sample weight. Besides, considering the weight of precursor and the carbon nanotubes the layer numbers of the fabricated polymer were 2-3 layers. the inconsistency proposes that, during the synthesis carbon nanotubes formed bundles, leading to a considerable decrease in the surface areas which infused significant surface area decline; therefore, the inherent nanopores of the carbon nanotubes were covering with polymers and not significantly inflected the N_2 adsorption.

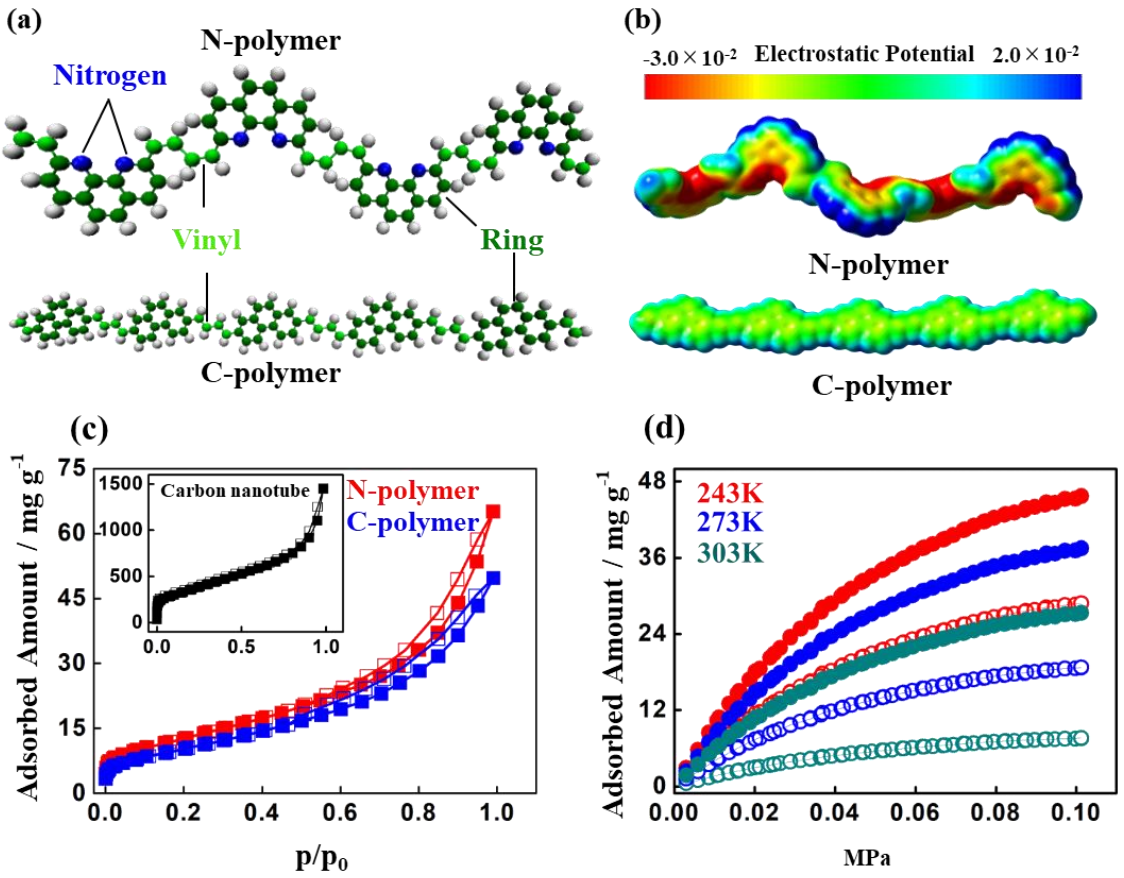

Figure 1. (a) Chemical structures of N-polymer and C-polymer using ball-and-stick models. Carbon, nitrogen, and hydrogen atoms are depicted by green, blue, and grey spheres, respectively. (b) Electrostatic potentials of N-polymer and C-polymer. (c) Nitrogen adsorption isotherms of carbon nanotube (inset), N-polymer, and C-polymer. (d) CO_2 adsorption isotherms of N-polymer (close symbols) and C-polymer (open symbols) at 243, 273, and 303 K.

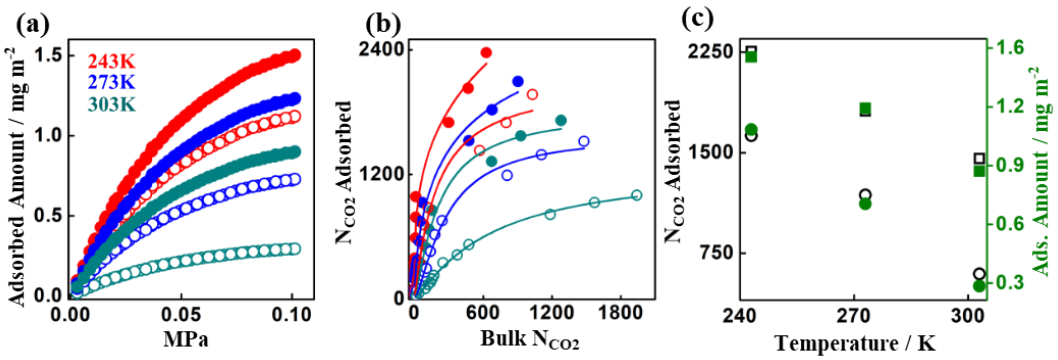

Figure 2. Experimental CO_2 adsorption isotherms per specific surface area (a) and simulated CO_2 adsorption amounts (b) on C-polymer (open symbols) and N-polymer (close symbols) at 243 K (red), 273 K (blue), and 303 K (green). (c) Temperature-dependent adsorption amounts of CO_2 on C-polymer (●) and N-polymer (■) in simulations for 600 bulk CO_2 molecules (black) and experiments at 0.1 MPa (green).

The Freundlich-type CO_2 adsorption isotherms were observed in Figure 1d. N-polymer adsorbed extensively higher amounts of CO_2 rather than C-polymer, although the specific surface area was similar. Figure 2a shows the per surface area CO_2 adsorption isotherms these were calculated from the adsorption isotherms and specific surface area of N-polymer and C-polymer, since the pristine adsorption isotherms on those polymers were not distinguishable. At 0.1 MPa, N-polymer adsorbed 1.5, 1.2, and 0.9 mg m^{-2} at 243, 273, and 303 K, respectively. Whereas the adsorbed amounts on C-polymer were 1.1, 0.7, and 0.3 mg m^{-2}, respectively. With the decreasing of temperature, the CO_2 adsorption amounts increased for N-polymer and C-polymer, which is an orthodox behavior for almost all of the adsorbents. The CO_2 adsorption performance of N-polymer was better than C-polymer, at different temperature 243, 273 and 303 K compare with C-polymer, N-polymer showed 40%, 70% and 200% higher

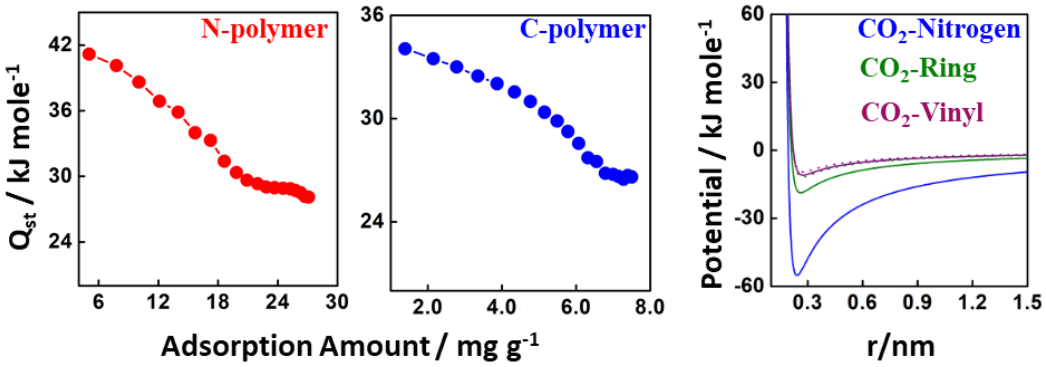

Figure 3. Experimental heat of adsorption of CO_2 on N-polymer (a) and C-polymer (b). Theoretical interaction potential of CO_2 to nitrogen (blue), CO_2 to ring (green) and CO_2 to vinyl (purple). Solid lines are for N-polymer and dotted lines are for C-polymer.

CO_2 uptake respectively. This suggested that N-polymer exhibited strong adsorption sites. Figure 2b shows the CO_2 adsorption phenomenon elucidated from the MD simulations, CO_2 adsorptions were calculated on a graphene fabricated by the polymers. The experimental CO_2 adsorption on N-polymer and the simulation adsorption outputs had the similar temperature dependency and increment. The change of the experimental and simulated CO_2 adsorption as a function of the temperature were depicted in figure 2c. The experimental amount was obtained at 0.1 MPa, while for 600 molecules in the bulk for the simulated amount. The adsorption amounts of the both polymers have been decreased with the increase of the temperature. Unlike C-polymer, the decreasing rates of CO_2 adsorption amount with temperature in N-polymer were moderate due to the strong adsorption potential. On the other hand, this difference became larger at higher temperature rather than lower temperature. Owing to the strong Coulombic interaction of CO_2 towards N-polymer, the CO_2 adsorption phenomenon were rarely changed.

The experimental heat of adsorption of CO_2 on N-polymer and C-polymer were calculated in figure 3 (a) and (b) by using following Clausius-Clapeyron equation-

$$\ln(P) = -\frac{q_{st}}{RT} + C \quad (1)$$

Were q_{st} was the heat of adsorption, P was pressure and T was temperature. The value of q_{st} was higher for N-polymer rather than C-polymer at lower CO2 coverage. These values for N-polymer was (41 – 27 kJ mol^{-1}) while for C-polymer was (34 – 26 kJ mol^{-1}). Compare to the C-polymer the higher value of q_{st} for N-polymer at lower coverage indicates a very favorable interaction between CO_2 and N-polymer. The binding interaction of CO_2 decrease at higher coverage since the favorable sites of N-polymer i.e. the nitrogen sites become occupied at lower pressure, which means nitrogen sites of N-polymer has the higher accessibility of CO_2. While C-polymer has relatively lower q_{st} value at lower CO_2 coverage due to the absence of nitrogen site. Similar results can also be seen from the theoretical results shown in the figure 3 (c) for the interaction potential between CO_2 and different sites of the polymers. The interaction potential for CO2-nitrogen site was -58 kJ mol^{-1} at a distance of 0.27 nm and -19 and -11 kJ mol^{-1} for ring and vinyl sites. While for C-polymer -12 and -9 kJ mol^{-1} for ring and vinyl sites respectively.

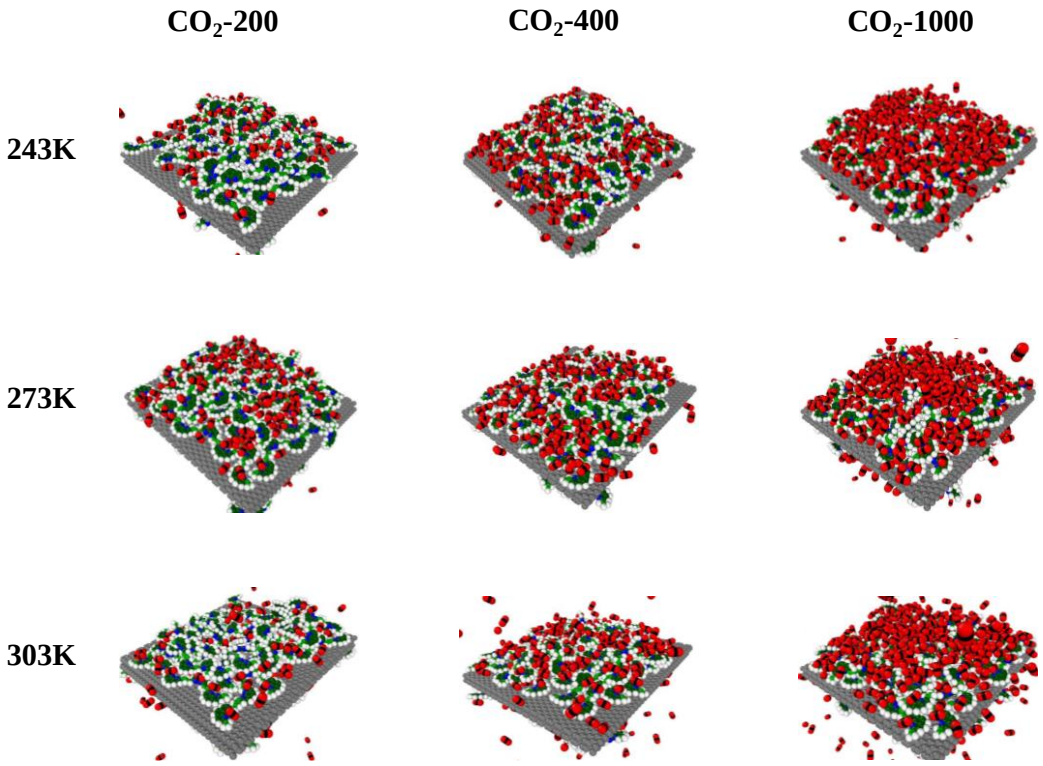

Figure 4. Snapshots of 400–2000 CO_2 molecules on N-polymer fabricated on two layer graphene at 243, 273, and 303 K.

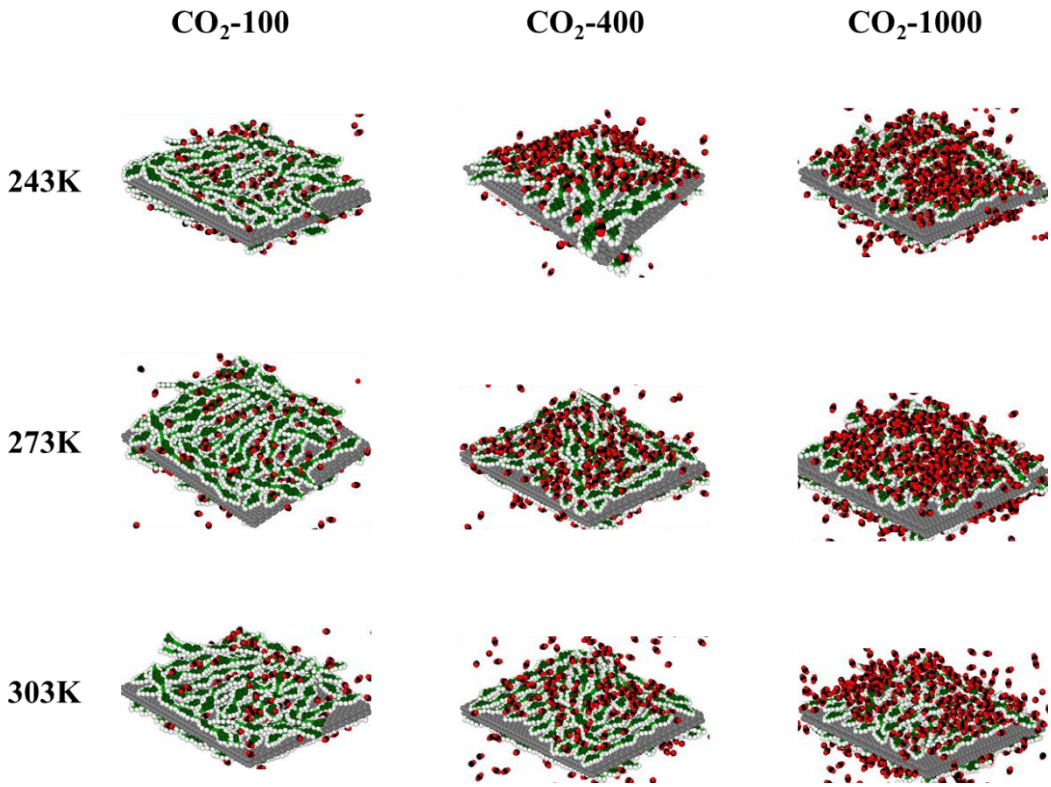

Figure 5. Snapshots of 400–2000 CO_2 molecules on C-polymer fabricated on two layer graphene at 243, 273, and 303 K

Figure 4 and figure 5 present snapshots of the CO_2 adsorbed on N-polymer and C-polymer respectively. The number of CO_2 adsorbed on the surface are temperature depended for both polymers. However, the number of adsorbed CO_2 is much higher in N-polymer rather than C-polymer at any conditions. Furthermore, significant CO_2 adsorption by nitrogen sites of N-polymer can be shown.

The simulated snapshots depicted in the figure 6a showed, in the side view CO2 were homogeneously distributed on both N-polymer and C-polymer, however, in the top views CO_2 were mainly adsorbed on the nitrogen and ring sites of N-polymer, while for C-polymer only adsorbed on the ring sites. There were three different adsorption sites in N-polymer such as nitrogen, ring and vinyl sites, on the other hand only ring and vinyl sites were in C-polymer. In figure 6b, to determine the active sites of both polymers for CO_2 adsorption the simulated radial distribution function was calculated between CO_2 and adsorption sites. In case of N-polymer the nearest-neighbor distance for CO_2 to nitrogen site was 0.31 nm, for CO_2 to ring it was 0.35 nm and 0.37 nm for CO_2 to vinyl site. On the other hand, for C-polymer 0.34 nm was nearest neighbor distance for CO_2 to ring and 0.37 nm for CO_2 to vinyl. Owing to largest negative partial charge in the nitrogen site of N-polymer, the CO_2 to nitrogen site distance was appeared in a shortest position, nitrogen site of N-polymer strongly attracting the positive charge of CO_2. According to the snapshots from MD simulations a CO_2 molecule was preferentially placed in the center of two nitrogen atoms. N-polymer and C-polymer had similar distances for CO_2 to ring and CO_2 to vinyl groups; however, the CO_2 to ring distance for N-polymer was somewhat greater than that for C-polymer because after adsorption of CO_2 on nitrogen sites of N-polymer the ring periphery space of N-polymer was less than that of C-polymer. According to the figure 2b carbon atoms on ring groups of C-polymer had slight negative charges, whereas carbon atoms for N-polymer had non-uniform charges, in spite of the heterogeneous charge distributions, the CO_2 to carbon groups distance was not changed, which proposed that instead of Coulombic interaction CO_2 adsorption on carbon groups was dominated by a dispersion interaction. the carbon ring site demonstrated higher interaction forces as it possessed high atomic

density compared to the vinyl site. Additionally, in case of the C-polymer the CO_2 to vinyl peaks were demolished since vinyl group had weaker interaction force. The intensity of radial distribution peaks was decline with the raising of the temperature, while in case of N-polymer these peaks were remain unchanged.

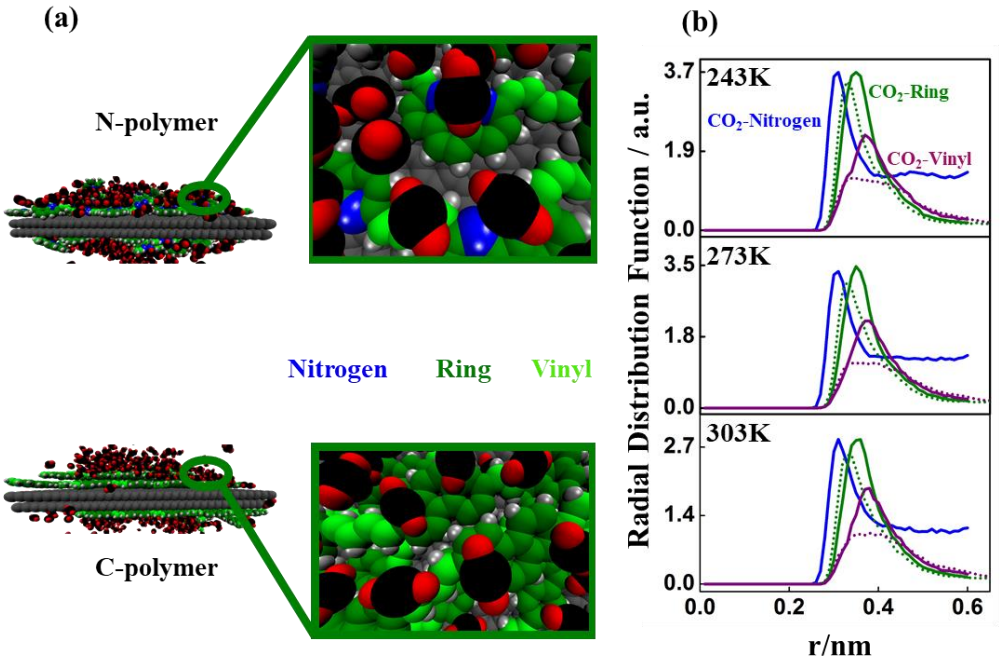

Figure 6. (a) Simulated snapshots after adsorption of CO_2 on N-polymer and C-polymer (Side and Top view). (b) Radial distribution functions for CO_2 nitrogen (blue), ring (green), and vinyl sites (purple) at 243, 273, and 303 K. The solid curves represent N-polymer, and the dotted curves represent C-polymer.

The mean square displacement and self-diffusion coefficient were calculated at different temperature from MD simulation to evaluate the change of the dynamics as a function of temperature, simulated CO_2 trajectories of the systems possess 300 CO_2 molecules

were considered to calculate the mean square displacement as depicted in figure 7. Apparently smaller mean square displacements were found for the CO_2 adsorbed on the nitrogen sites of N-polymer compared to the ring and vinyl sites of both polymers. According to the figure 7 With the increase of temperature, the mean square displacements of CO_2 molecules in the vicinity of ring and vinyl sites of N-polymer and C-polymer, were increased, while that in the vicinity of nitrogen sites was relatively constant. In the applied temperature range CO_2 adsorbed on the nitrogen sites of N-polymer was strongly connected to nitrogen atoms, whereas with increase temperature more than 273 K CO_2 adsorbed on ring and vinyl sites were released and the mean square displacement was close to that of C-polymer.

Figure 8 shows the change of the self-diffusion coefficients were calculated from the equation 2

$$\mathrm{D} = \langle \big(R(t) - R(0)\big)^2 \rangle / 6t \,, \qquad (2)$$

where D is the self-diffusion coefficient and $R(t)$ is the position vector of CO_2 at time t. With the raising of the temperature the self-diffusion coefficients of CO_2 adsorbed on nitrogen sites of N-polymer were increased adequately while CO_2 adsorbed on ring and vinyl sites had opposite phenomenon.

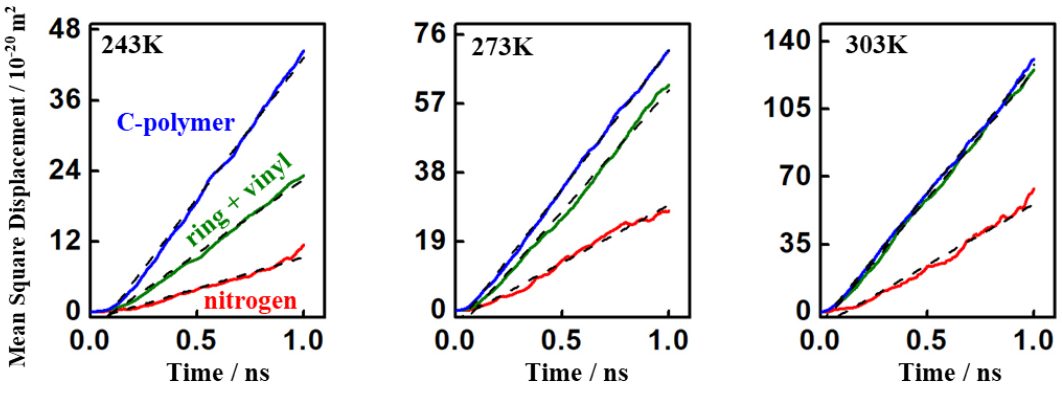

Figure 7. Mean square displacement of CO_2 versus time on the nitrogen sites of N-polymer (red curves) and on the ring and vinyl sites of N-polymer (green curves) and C-polymer (blue curves) at 243 K, 273 K, and 303 K. Fitting lines were depicted by dashed black line.

C-polymer had higher self-diffusion coefficients near the ring and vinyl sites than those of N-polymer. However, at 303 K temperature the self-diffusion coefficients in the vicinity of ring and vinyl sites of N-polymer and C-polymer were similar. The weak attraction formed by the Coulombic interaction between CO_2 and ring or vinyl group was defeated by the accelerated kinetic energy of CO_2. The kinetic energy significantly decreased due to the strong attraction of the nitrogen sites toward CO_2. Therefore, the negatively charged nitrogen sites of N-polymer played an important role to decline the self-diffusion coefficient of the CO_2 and retain the adsorption amounts. At higher temperature nitrogen sites mainly facilitated the significant CO_2 adsorption by retaining CO_2 dynamics, while at lower temperature ring and vinyl sites were contributed for CO_2 adsorption, which also can be seen in the Figure 2a–2c.

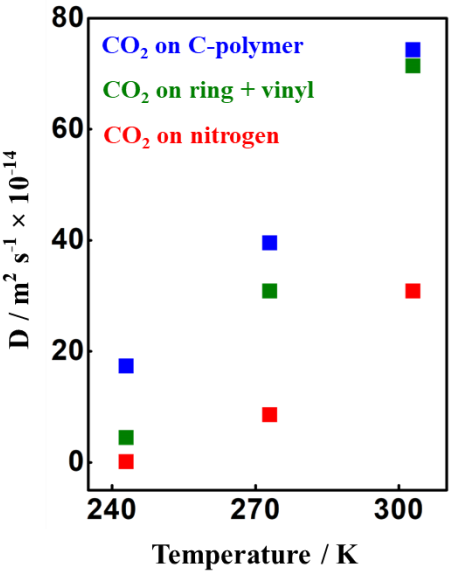

Figure 8. Self-diffusion coefficients of CO_2 near ring and vinyl sites of C-polymer (blue) and near nitrogen sites (red) and ring and vinyl sites (green) of N-polymer at 243, 273, and 303 K.

Remarkable CO_2 adsorption and reduction of CO_2 dynamics were observed on N-polymer, and CO_2 was adsorbed reversibly. This kind of strong and reversible adsorption of CO_2 are useful for high performative CO_2 sensors.

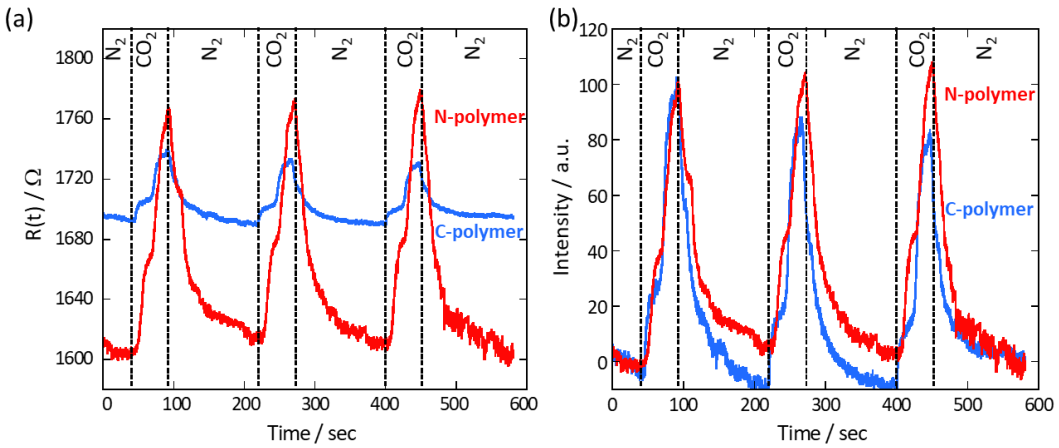

Figure 9. (a) Resistance changes and (b) normalized resistance changes for the first peaks of N- and C-polymers with CO_2 introduction.

The change of the resistance of the polymer in CO_2 and nitrogen conditions as a function of time were depicted in figure 9a. With the introduction of the CO_2 the resistances of both N-polymer and C-polymer raised. The Lewis acidic character of the CO_2 induced it to act as electron acceptor from the basic nitrogen site of N-polymer or in case of C-polymer from the ring and vinyl sites. Both N-polymer and C-polymer were thus act as a n-type semiconductor. The normalized relative resistances were illustrated in the figure 9b. As can be expected from the self-diffusion coefficient figure 8, N-polymer demonstrated slower resistance recovery after the introduction of the nitrogen rather than the C-polymer, this is because the dynamics of the CO_2 molecules were restricted by the nitrogen sites. However, C-polymer normalized peaks were declined gradually while in case of N-polymer peaks were maintained. This was an unexpected finding since chemisorption and/or strong physical adsorption typically impose a reduction of resistance change. Despite reversible adsorption was observed, CO_2 was thus strongly adsorbed on N-polymer.

In the Figure 10 the relative resistance changes were calculated from the differential between the resistances at *t* and 0 s. The relative resistance change of C-polymer was approximately 2%, which is similar to that for reported carbon sensors.[57-58] . In case of N-polymer, five times larger resistance change was achieved than that for C-polymer, the change was up to 10 %. The extensive adsorption of the CO_2 on nitrogen groups and the electron transformation between nitrogen group to CO_2 molecules mostly facilitated the huge resistance changes. The first steps of the resistance changes

for N-polymer and C-polymer were approximately 4% and 0.5% respectively with CO_2 introduction. The first step of the resistance change was observed instantaneously after switching gases. The electrical resistance could be influenced by changing the pressure as well as through adsorption. We expected pressure change and adsorption induced the, respectively. Therefore, the first and second steps were mainly attributed to pressure fluctuation and adsorption, respectively.

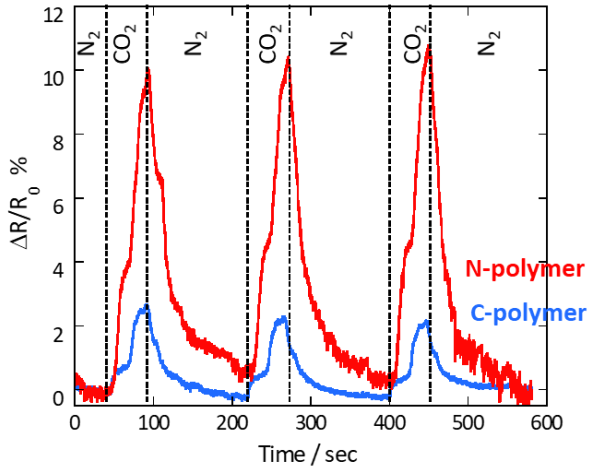

Figure 10. Response curves to CO_2 introduction on N-polymer and C-polymer.

In the CO_2 environment retention of the CO_2 adsorption amounts facilitated the outstanding cyclability while during the CO_2 adsorption and desorption the structural change of the N-polymers were avoided and from self-heating due to the low resistivity during the measurements. CO_2 adsorption and desorption induced the structural change of the flexible polymer, and with the repeating of cycles its adsorption changes gradually decreased.[59] Thus in the Figure 11, mean square displacement of the N-polymer and C-polymer were depicted in order to elucidate the structural changes of the N-polymer and C-polymer. The structural change of the N-polymer was more

maintained rather than C-polymer during the CO_2 adsorption. Therefore, we assumed that the CO_2 sensing performance of C-polymer was little decreased due to its flexible structure instead of self-heating, since N-polymer and C-polymer had small resistance differences.

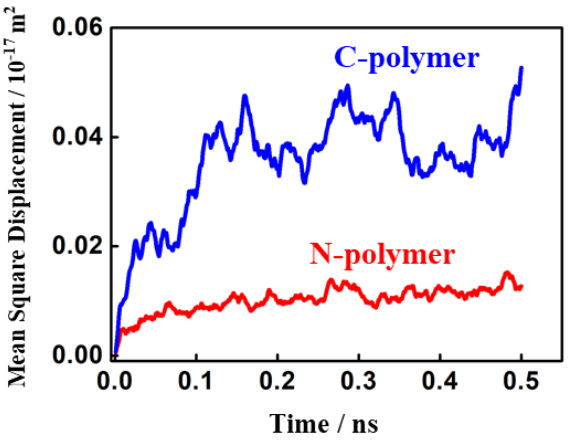

Figure 11. Mean square displacement of N- and C-polymers during CO_2 adsorption. CO_2 was introduced at 0.0 ns.

3.4. Conclusion

This study comprehensively elucidated the CO_2 adsorption and sensing properties of a nitrogen containing polymer and a polymer without nitrogen atoms, in order to evaluate the correlation between nitrogen atoms on a polymer and CO_2. In case of N-polymer due to the presence of highly electronegative nitrogen atoms, N-polymer consist heterogeneous partial charge distribution, while in the C-polymer has almost neutral change distribution. CO_2 molecules works as a weak Lewis acid even though it has both positive carbon and negative oxygen atoms and shows significantly higher

attractions towards nitrogen sites. Both experimental CO_2 adsorption isotherms and MD simulation adsorption phenomenon suggested that N-polymer consist higher CO_2 uptakes rather than C-polymer at considered temperature 243, 273 and 303 K. CO_2 on N-polymer homogeneously distributed at temperature 243 and 273 K, while at 303 K mostly adsorbed on the nitrogen sites. The self-diffusion coefficient calculated from the MD simulation suggested that, CO_2 adsorbed on the nitrogen sites have smaller diffusion coefficient than those on ring and vinyl sites, while at higher temperature those were almost constant. N-polymer showed the high CO_2 gas sensing performance since CO_2 has strong attraction force with nitrogen sites and N-polymer has reduced structural change which provide sufficient reversibility. Thus, introduction of the nitrogen atoms on the polymer structure adequately improve the CO_2 adsorption capability and electrical conductivity as well as significantly higher CO_2 sensing performance.

References

(1) Nandi, M.; Uyama, H. Exceptional CO_2 Adsorbing Materials Under Different Conditions. *Chem. Rec.* **2014,** *14*, 1134-1148.

(2) Haszeldine, R. S. Carbon Capture and Storage: How Green Can Black Be? *Science* **2009,** *325*, 1647-1652.

(3) Monastersky, R. Global Carbon Dioxide Levels Near Worrisome Milestone. *Nature* **2013,** *497*, 13-14.

(4) Hinkov, I.; Lamari, F. D.; Langlois, P.; Dicko, M.; Chilev, C.; Pentchev, I. Carbon Dioxide Capture by Adsorption. *J. Chem. Technol. Metallurgy* **2016,** *51*, 609-626.

(5) White, C. M.; Smith, D. H.; Jones, K. L.; Goodman, A. L.; Jkich, S. A.; LacCount, R. B.; Ozdemir, E.; Morsi, B.I.; Schroeder, K. T. Sequestration of Carbon Dioxide in Coal with Enhanced Coalbed Methane Recovery, A Review. *Energy Fuels* **2005,** *19,* 659-725.

(6) Wang, W.; zhou, M.; Yuan, D. Carbon Dioxide Capture in Amorphous Porous Organic Polymers. *J. Mater. Chem. A* **2017,** *5,* 1334-1347.

(7) Liu, L.; Bhatia, S. K. Molecular Simulation of CO_2 Adsorption in the Presence of Water in Single-Walled Carbon Nanotubes *J. Phys. Chem. C* **2013,** *117,* 13479-13491.

(8) Himeno, S.; Komatsu, T.; Fujita, S. High-Pressure Adsorption Equilibrium of Methene and Carbon Dioxide on Several Activated Carbons. *J. Chem. Eng. Data* **2005,** *50,* 369-376.

(9) Hao, G. P.; Li, W. C.; Lu, A. H. Novel Porous Solids for Carbon Dioxide Capture. *J. Mater. Chem.* **2011,** *21*, 6447-6451.

(10) Zhu, X.; Hillensheim, P. C.; S. M. Mahurin; Wang, C.; Tian, C.; Brown, S.; Luo, H.; Veith, G. M.; Han, K. S.; Hagaman, E. W.; Liu, H.; Dai, S. Efficient CO_2 Capture by Porous, Nitrogen Doped Carbonaceous Adsorbents Derived from Task-specific Ionic Liquids. *ChemsusChem* **2012,** *5*, 1912-1917.

(11) Zhao, L.; Bacsik, Z.; Hedin, N.; Wei, W.; Sun, Y.; Antonietti, M.; Titirici, M. M. Carbon Dioxide Capture on Amine-Rich Carbonaceous Materials Derived from Glucose. *ChemsusChem* **2010,** *3,* 840-845.

(12) Sho, X.; Feng, Z.; Xue, R.; Ma, C.; Wang, W.; Peng, X.; Cao, D. Adsorption of CO_2, CH_4, CO_2/N_2 and CO_2/CH_4 in Novel Activated Carbon Based: Preparation, Measurements and Simulation. *AlChe J.* ***2011,*** *57,* 3042-3051.

(13) Wu, Z.; Hao, N.; Xiao, G.; L. Liu; Webley, P.; Zhao, D. One-pot Generation of Mesoporous Carbon Supported Nanocrystalline Calcium Oxides Capable of Efficient CO_2 Capture Over a Wide Range of Temperatures. *Phys. Chem. Chem. Phys.* **2011,** *13*, 2495-2503.

(14) Sumida, K.; Rogow, D. L.; Mason, J. A.; McDonald, T. M.; Bloch, E. D.; Herm, Z. R.; Bae, T. H.; Long, J. R. Carbon Dioxide Capture in Metal-Organic Frameworks. *Chem. Rev.* **2012,** *112*, 724-781.

(15) Fracaroli, A. M.; Furukawa, H.; Suzuki, M.; Dodd, M.; Okajima, S.; Gandara, F.; Reimer, J. A.; Yaghi, O. M. Metal-Organic Frameworks with Precisely Designed Interior for Carbon Dioxide Capture in the Presence of Water. *J. Am. Chem. Soc.* **2014,** *136*, 8863-8866.

(16) Cavenati, S.; Grande, C. A.; Rodrigues, A. E. Adsorption Equilibrium of Methene, Carbon Dioxide, and Nitrogen on Zeolite 13X at High Pressure *J. Chem. Eng. Data* **2004,** *49*, 1095-1101.

(17) Wang, Y.; LeVan, M. D. Adsorption Equilibrium of Carbon Dioxide and Water Vapor on Zeolites 5A and 13X and Silica Gel: Pure Components. *J. Chem. Eng. Data* **2009,** *54*, 2839-2844.

(18) Choi, S.; Drese, J. H.; Jones, C. W. Adsorption Materials for Carbon Dioxide Capture from Large Anthropogenic Point Sources. *ChemSusChem* **2009,** *2*, 796-854.

(19) Akhtar, F.; Liu, Q.; Hedin, N.; Bergstrom, L. Strong and Binder Free Structure Zeolite Sorbents with Very High CO_2-over-N_2 Selectivities and High Capacities to Adsorb CO_2 Rapidlly. *Energy Environ. Sci.* **2012,** *5*, 7664-7673.

(20) Foo, M. L.; Matsuda, R.; Hijikata, Y.; Krishna, R.; Sato, H.; Horike, S.; Hori, A.; Duan, J.; Sato, Y.; Kubota, Y.; Takata, M.; S. Kitagawa. An Adsorbate

Discriminatory Gate Effect in a Flaxible Porous Coordination Polymer for Selective Adsorption of CO_2 over C_2H_2. *J. Am. Chem. Soc.* **2016,** *138*, 3022-3030.

(21) Comotti, A.; Fraccarollo, A.; Bracco, S.; Beretta, M.; Distefano, G.; Cossi, M.; Marchese, L.; Riccardi, C.; Sozzani, P. Porous Dipeptide Crystals as Selective CO_2 Adsorbents: Experimental Isotherm vs. Grand Canonical Mote Carlo Simulations and MAS NMR Spectroscopy. *CrystEngComm* **2013,** *15*, 1503-1507.

(22) Hicks, J. C.; Drese, J. H.; Fauth, D. J.; Gray, M. L.; Qi, G.; Jones, C. W. Designing Adsorbents for CO_2 Capture from Flue Gas-Hyperbranched Aminosilicas Capable of Capturing CO_2 Reversibly. *J. Am. Chem. Soc.* **2008,** *130*, 2902-2903.

(23) Khatri, R. A.; Chuang, S. S. C.; Soong, Y.; Gray, M. Thermal and Chemical Stability of Regenerable Solid Amine Sorbent for CO_2 Capture. *Energy Fuels* **2006,** *20*, 1514-1520.

(24) Watanabe, T.; Khan, S. M.; Kanoh, H.; Ohba, T. Significant CO_2 Adsorption Ability of Nanoscale $BaTiO_3$ Ceramics Fabricated by Carbon-Template-Solvothermal Reactions. *Phys Chem Ind J.* **2017**, S1: 101

(25) An, H.; Feng, B.; Su, S. CO_2 Capture by Electrothermal Swing Adsorption with Activated Carbon Fibre Materials. *Int. J. Greenhouse Gas Control* **2011,** *5*, 16-25.

(26) Hutson, N. D.; Speakman, S. A.; Payzant, E. A.; Structural Effects on the High Temperature Adsorption of CO_2 on a Synthetic Hydrotalcite. *Chem. Mater.* **2004,** *16*, 4135-4143.

(27) Takamura, Y.; Narita, S.; Aoki, J.; Hironaka, S.; Uchida, S. Evaluation of Dual-Bed Pressure Swing Adsorption for CO_2 Recovery from Boiler Exhust Gas. *Sep. Purif. Technol.* **2001,** *24*, 519-528.

(28) Grande, C. A.; Rodrigues, A. E. Electric Swing Adsorption for CO_2 Removal from Flue Gases. *Int. J. Greenhouse Gas Control* **2008,** *2*, 194-202.

(29) Ben, T.; Ren, H.; Ma, S.; Cao, D.; Lan, J.; Jing, X.; Wang, W.; Xu, J.; Deng, F.; Simmons, J. M.; Qiu, S.; Zhu, G. Targeted Synthesis of a Porous Aromatic Framework with High Stability and Exceptional High Surface Area. *Angew. Chem., Int. Ed.* **2009,** *48*, 9457-9460.

(30) Ren, H.; Ben, T.; Sun, F.; Guo, M.; Jing, X.; Ma, H.; Cai, K.; Qiu, S.; Zhu, G. Synthesis of a Porous Aromatic Framework for Adsorbing Organic Pollutants Application. *J. Mater. Chem.* **2011**, *21*, 10348-10353.

(31) Ben, T.; Pei, C.; Zhang, D.; Xu, J.; Deng, F.; Jing, X.; Qiu, S. Gas Storage in Porous Aromatic Frameworks (PAFs). *Energy Environ. Sci.* **2011,** *4*, 3991-3999.

(32) Ren, H.; Ben, T.; Wang, E.; Jing, X.; Xue, M.; Liu, B.; Cui, Y.; Qiu, S.; Zhu, G. Targated Synthesis of a 3D Porous Arometic Framework for Selective Sorption of Benzene. *Chem. Commun.* **2010,** *46*, 291-293.

(33) Yuan, Y.; Sun, F.; Ren, H.; Jing, X.; wang, W.; Ma, H.; Zhao, H.; Zhu, G. Targeted Synthesis of a Porous Aromatic Framework with a High Adsorption Capacity for Organic Molecules. *J. Mater. Chem.* **2011,** *21*, 13498-13502.

(34) Cong, H. L.; Zang, M.; Chen, Y.; Chen, K.; Hao, Y.; Zhao, Y.; Feng, L. Highly Selective CO_2 Capture by Nitrogen Enriched Prous Carbon. *Carbon* **2015,** *92*, 297-304.

(35) Srinivas, G.; Krunglevicitute, V.; Guo, Z.; Yildirim, T. Exceptional CO_2 Capture in a Hierarchically Porous Carbon with Simultaneous High Surface Area and Pore Volume. *Energy Environ. Sci.* **2014,** *7*, 335-342.

(36) Wang, J.; Senkovska, I.; Oschatz, M.; Lohe, M. R.; Borchardt, L.; Heerwing, A.; Liu, Q.; Kaskel, S. Imine-Linked Polymer-Derived Nitrogen-Doped Microporous

Carbons with Excellent CO_2 Capture Properties. *ACS Appl. Mater. Interfaces* **2013,** *5*, 3160-3167.

(37) Chen, Q.; Luo, M.; Hammershoj, P.; Zhou, D.; Han, Y.; Laursen, B. W.; Yan, C. G.; Han, B. H. Microporous Polycarbazole with High Specific Surface Area for Gas Storage and Separation. *J. Am. Chem. Soc.* **2012,** *134*, 6084-6087.

(38) Hug, S.; Mesch, M. B.; Oh, H.; Popp, N.; Hirscher, M.; Senker, J.; Lotsch, B. V. A Fluorene Based Covalent Triazine Franework with High CO_2 and H_2 Capture and Storage Capacities. *J. Mater. Chem. A* **2014,** *2*, 5928-5936.

(39) Rabbani, M. G.; El-Kaderi, H. M. Synthesis and Characterization of Porous Benzimidazole Linked Polymers and Their Performance in Small Gas Storage and Selective Uptake. *Chem. Mater.* **2012,** *24*, 1511-1517.

(40) Rabbani, M. G.; El-Kaderi, H. M. Template-Free Synthesis of a Highly Porous Benzimidazole-Linked Polymer for CO_2 Capture and H_2 Storage. *Chem. Mater.* **2011,** *23*, 1650-1653.

(41) Li, Q.; Yang, J.; Feng, D.; Wu, Z.; Wu, Q.; Park, S. S.; Ha, C.; Zhao, D. Facile Synthesis of Porous Carbon Nitride Spheres with Hierarchical Three-Dimensional Mesostructures for CO_2 Capture. *Nano Res.* **2010,** *3*, 632-642.

(42) Maroto-Valer, M. M.; Tang, Z.; Zhang, Y. CO_2 Capture by Activated and Impregnated Anthracites. *Fuel Process. Technol.* **2005,** *86*, 1487-1502.

(43) Xing, W.; Liu, C.; Zhou, Z.; Zhang, L.; Zhou, J.; Zhuo, S.; Yan, Z.; Gao, H.; Wang, G.; Qiao, S. Z. Superior CO_2 Uptake of N-doped Activated Carbon Through Hydrogen-bonding Interaction. *Energy Environ. Sci.* **2012,** *5*, 7323-7327.

(44) Sevilla, M.; Parra, J. B.; Fuertes, A. B. Assesment of the Role of Micropore Size and N-Doping in CO_2 Capture by Porous Carbons. *ACS Appl. Mater. Interfaces* **2013,** *5*, 6360-6368.

(45) Kumar, K. V.; Preuss, K.; Lu, L.; Guo, Z. X.; Titrici, M. M. Effect of Nitrogen Doping on the CO_2 Adsorption Behavior in Nanoporous Carbon Structures: A Molecular Simulation Study. *J. Phys. Chem. C* **2015,** *119*, 22310-22321.

(46) Yamada, Y.; Gohda, S.; Abe, K.; Togo, T.; Shimano, N.; Sasaki, T.; Tanaka, H.; Ono, H.; Ohba, T.; Kubo, S.; Ohkubo, T.; Sato, S. Carbon Materials with Controlled Edge Structures. *Carbon* **2017,** *122*, 694-701.

(47) Hata, K.; Futaba, D. N.; Mizuno, K.; Namai, T.; Yumura, M.; Iijima, S., Water-Assisted Highly Efficient Synthesis of Impurity-Free Single-Walled Carbon Nanotubes. *Science* **2004,** *306*, 1362-1362.

(48) Barrett, E. P.; Joyner, L. G.; Halenda, P. P. The Determination of Pore Volume and Area Distributions in Porous Substances. I. Computaions from Nitrogen Isotherms. *J. Am. Chem. Soc.* **1951,** *73*, 373-380.

(49) Martinez, L.; Andrade, R.; Birgin, E. G.; Martinez, J. M. PackMOL: A Package for Building Initial Configurations for Molecular Dynamics Simulations. *J. Comput. Chem.* **2009,** *30*, 2157-2164.

(50) Martinez, J. M.; Martinez, L. Packing Optimization for Automated Generation of Complex System`s Initial Configurations for Molecular Dynamics and Docking. *J. Comput. Chem.* **2003,** *24*, 819-825.

(51) Ohba, T. The Thinnest Molecular Seperation Sheet by Graphene Gates of Single-Walled Carbon Nanohorns. *ACS Nano* **2014,** *8*, 11313-11319.

(52) Potoff, J. J.; Siepmann, J. I. Vapor-Liquid Equilibria of Mixtures Containing Alkanes, Carbon Dioxide and Nitrogen. *AlChE J.* **2001,** *47, 1676-1682*.

(53) Wang, J.; Wang, W.; Kollman, P. A.; Case, D. A. Automatic Atom Type and Bond Type Perception in Molecular Mechanical Calculations. *J. Mol. Graph. Model.* **2006,** *25*, 247-260.

(54) Wang, J.; Wolf, R. M.; Caldwell, J. W.; Kollman, P. A.; Case, D. A. Development and Testing of General Amber Force Field. *J. Comput. Chem.* **2004,** *25*, 1157-1174.

(55) Wang, L.; Yang, R. T. Significantly Increased CO_2 Adsorption Performance of Nanostructured Templated Carbon by Tuning Surface Area and Nitrogen Doping. *J. Phys. Chem. C* **2012,** *116*, 1099-1106.

(56) Thommes, M.; Kaneko, K.; Neimark, L. V.; Olivier, J. P.; Rodriguez-Reinoso, F.; Rouquerol, J.; Sing, K. S. W. Physisorption of Gases, with Special Reference to the ecaluation of Surface Area and Pore Size Distribution (IUPAC Technical Report). *Pure Appl. Chem.* **2015,** *87*, 1051-1069.

(57) Zhou, Y.; Jiang, Y. D.; Xie, T.; Tai, H. L.; Xie, G. Z. A Novel Sensing Mechanism for Resistive Gas Sensors Based on Layered Reduced Graphene Oxide Thin Films at Room Temperature. *Sensor Actuat B-Chem* **2014,** *203*, 135-142.

(58) Fan, X.; Elgammal, K.; Smith, A. D.; Östling, M.; Delin, A.; Lemme, M. C.; Niklaus, F. Humidity and CO_2 Gas Sensing Properties of Double-Layer Graphene. *Carbon* **2018,** *127*, 576-587.

(59) Choi, H. S.; Suh, M. P. Highly Selective CO_2 Capture in Flexible 3D Coordination Polymer Networks. *Angew. Chem. Int. Ed.* **2009,** *48*, 6865-6869.

Chapter 4

Anomalous Changes of Intermolecular Distance in Aqueous Electrolytes in Narrow Pores of Carbon Nanotubes

4.1 Introduction

Nanospace confined electrolytes have unique structural properties. Comprehensive understandings of those are crucial to develop efficient and cost-effective technologies in electrochemistry and to resolve the different mechanism in biochemistry. Electrical double-layer capacitors (EDLCs) have been considered as promising energy storage devices because of impressive high-power densities, unique cycle life, stability and reliability. EDLCs store energy by charge accumulation in the electric double layer.[1] Effective EDLC design optimization is a significant challenge due to the hypocritical relationship between electrode and electrolyte properties, and considerable influence of their on the overall performance, optimization of effective EDLC design is extensively challenging.[2-5] In last few decade different kinds of electrolytes have been reported in order of attain high performance of EDLC, among these electrolytes aqueous electrolyte provides higher power density owing to relatively low equivalent series resistance and high relative permittivity.[6] Different materials, including activated carbons,[7-10] carbon nanotubes (CNTs),[11-12] templated porous carbons[13-15] and carbon nanofibers[16] are used as EDLC electrodes.[17-19]

Owing to large exposed surface area as well as high electrical conductivity and electrochemical stability CNTs have been considered a promising electrode material.

CNTs could be a standard one-dimensional nanospaces system for the investigation of the behaviour of electrolyte solutions in one-dimensional nanospaces.[20] X-ray absorption fine structure analysis has been used by Ohkubo et al. to elucidate the hydration number of the ions in the hydrophobic nanospaces.[21-22] Despite experimental evaluation, several numbers of computational works as mentioned above have been carried out to clarify the detailed structures and mechanism. Feng et al proposed Na^+ and Cl^- ions required eight-time higher free energy to overcome to enter into CNT pores of diameter 0.82 nm rather than 0.82 nm slit pores.[23] The simulation suggested that in a CNT the preferential orientation of water molecules in the coordination shell of Na^+ and K^+ differed considerably from that in bulk solution.[24] Using molecular dynamics (MD) simulations Shao et al. also proposed that CNTs with diameters smaller than 0.87 nm provided strong hydration shells.[25] However, experimental and simulation have been separately conducted and had weak relation with each other. In order to have comprehensive understandings of the mechanism and improve the application, and elucidate the incompatibility between experiment and simulation, the collaborative study of experiment and simulation on aqueous solution in CNTs is thus necessary.

The aim of this chapter of this thesis is to elucidate the experimental and simulated structure of LiCl and NaCl aqueous electrolyte solutions in CNT pores in 1 nm diameter (1 nm CNTs) and CNT pores in 2 nm diameter (2 nm CNTs) by using X-ray diffraction (XRD) and MD simulations techniques. Moreover, the structural properties of these electrolytes have been compared with the structure of water inside the different diameter of CNTs.

4.2 Experimental and Simulation Procedures

The super growth method (Hata group, AIST, Ibaraki, Japan) and high-pressure carbon mono-oxide method (Unidym Inc., Menlo Park, CA) were used for synthesizing the 1 nm and 2 nm CNTs used in this study. Combination of transmission electron microscopy and N_2 adsorption isotherms techniques were used to determine the diameter distribution of the used CNTs, the details were explained elsewhere.[26-27] Firstly, The LiCl and NaCl aqueous solutions were prepared with 0.5 M concentration and CNTs were immersed in those solutions for more than 1 week. Secondly, the immersed CNTs were collected by filtration of the aqueous solutions, simultaneously deionized water flowed to remove the adsorbed electrolytes from the external surface of the CNTs. To compare the electrolytes structure with bulk water, only water adsorbed CNT samples were prepared by following same procedure. After filtration, 0.5 mm diameter of capillary glass tubes were used to collect the CNTs promptly. Before final sealing of the samples in tubes, the water adsorbed on the CNTs external surface from the deionized water was used for washing during filtration had to be removed, for this the samples were introduced to 85% humid atmosphere for 2 days. To measure the synchrotron XRD patters of water, NaCl and LiCl aqueous solution adsorbed CNTs as well as the bare CNTs, we used SPring-8 synchrotron radiation facility. The XRD data for all samples were collected for 20 min after introduction with BL02B2 beamline with the wavelength 0.09995 nm at the temperature of 303 K.

For simulations there are several frameworks have been reported, however in order to describe the condensed systems molecular phenomenon MD simulation has been

considered as most suitable framework .[28] First principle methods are highly computationally expensive to conduct the large scale calculations.[29-33] Since, the systems studies in this chapter were relatively big systems with some thousands of atoms, therefore MD simulations were used in this study. Large-scale Atomic/Molecular Massively Parallel Simulator (LAMMPS) molecular dynamics code was used to perform MD simulations. The initial configuration of the simulation systems were prepared by using Packmol and moltemplete.[34-35] Particle mesh Ewald sum were used to perform long ranged coulombic interaction with a real space cut off of 1.2 nm. In order to calculate the long ranged coulombic interactions particle mesh Ewald sum were used the cut off of 1.2 nm. 5 nm length single wall CNTs were considered with the diameter of 1.1 to 2.1 nm, while the effective diameters were 0.66 to 1.66 nm. The two ends of the CNTs were embedded in to two different graphene sheets having pore similar with the diameters of CNT, this type of setup helped to avoid the adsorption of the molecules on the external surface of the CNTs. The initial position of the graphene and CNTs were kept fixed during the simulations. The 12-6 Lennard-Jones potential parameters of CNTs were σ_C= 0.342 nm and ε_C = 0.2506 kJ mol^{-1} with 0.142 nm distance.[36] Parameters of the TIP4P model of water are σ_H = 0.00 nm, σ_O = 0.3164 nm, ε_H = 0.00 kJ mol^{-1} and ε_O = 0.6809 kJ mol^{-1}, which is highly consistent with the reproducibility of the experimental dielectric constant of water.[37] In order to kept the O-H bonds and H-O-H angle of water fixed SHAKE algorithm was used.[38] Parameter for Lennard-Jones potentials of different ions were σ_{Li} = 0.213 nm, σ_{Na} = 0.3333 nm, σ_{Cl} = 0.442 nm, and ε_{Li} = 0.0765 kJ mol^{-1}, ε_{Na} = 0.0116 kJ mol^{-1}, ε_{Cl} = 0.4930 kJ mol^{-1}.[24] The ions in the systems were constructed with standard electrostatic charge. To calculate the all cross Lennard-Jones interaction between all of the molecules, Lorentz-

Berthelot mixing rules were employed. All the system constructed with 1829 water molecules, 36 Li or Na ions and 36 Cl ions, all of the ions and molecules were randomly placed in the both entrance of CNTs. NPT ensembled simulations were adopted for 2 ns of the all systems at pressure 0.1 MPa, which allowed the electrolytes to enter into the CNTs and provide atmospheric pressure condition. Then NVT ensembled simulations were performed for 2 ns at 298 K temperature and the time step was 1 fs. The temperature was maintained during NVT simulation by using the Nosé-Hoover algorithm.

4.3 Results and discussion

Figure 1 shown the XRD patterns of LiCl and NaCl aqueous electrolyte solutions-adsorbed CNTs, and bare CNTs. In order of comparison the XRD patterns of only water adsorbed CNTs were also included. The scattering parameter *s* is defined as $4\pi \sin(\theta)/\lambda$. The scattering intensities for aqueous electrolyte solutions and water-adsorbed CNTs were certainly increased from those of bare CNTs, particularly from 7–30 nm^{-1}, which means that a numerous amount of aqueous electrolyte solution or water was adsorbed in CNTs. The patterns of those scattering of aqueous electrolyte- and water-adsorbed CNTs were also distinguishable from each other in the range of 7–20 nm^{-1}. This expressed that electrolyte nanostructure and water nanostructure in CNTs were different.

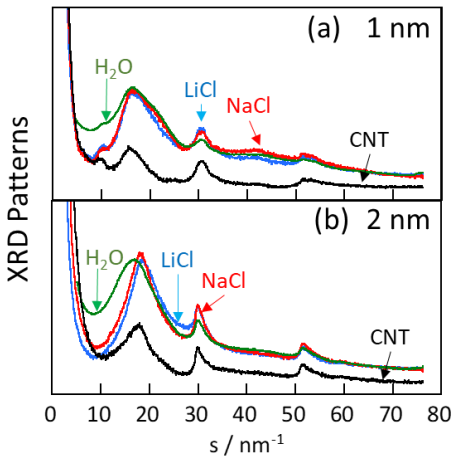

Figure 1 XRD patterns of aqueous electrolyte solutions- and water-adsorbed in CNTs of averaged diameter 1 nm (a) and 2 nm (b), and bare CNTs (CNTs in vacuum).

The XRD patterns of 1nm and 2 nm CNTs systems for aqueous electrolytes and water were attained from the subtraction from the aqueous electrolytes or water and bare CNTs XRD pattern as shown in the figure 2. First, we assumed that the scattering intensity of adsorbed electrolytes corresponded to the scattering intensity difference between CNT adsorbed electrolyte and bare CNT in the large scattering parameter, and secondly adsorption amounts were used to adjust the scattering intensity to the expected one. Due to the peaks of residual CNT the assumption of adjusting peak intensity for electrolyte solutions might bring the error, various intensity ratio between CNT adsorbed electrolytes and bare CNT were considered to examine the possible XRD patterns and electron radial distribution functions (ERDFs), as depicted in Figure 3. The shapes of XRD and ERDF patterns were little bit changed by the various intensity ratio despite the obvious change of the intensity ratio. However, in details ERDF analyses were explained later. Electrolyte–CNTs, and water–CNTs scatterings were somewhat remained in those subtracted XRD patterns. The XRD patterns in 1 nm CNTs reported

that the first peaks appeared at 20 nm^{-1} were perfectly forgathered with each other, while the second peak appeared around 45 nm^{-1} for NaCl aqueous solution in 1 nm CNT was little bit stronger rather than LiCl aqueous solution and water. Those similarities may be because the small nanopore like 1 nm CNTs can allow only few ions to be entered. However, in case of 2 nm CNTs systems significant difference can be seen between the XRD patterns for water, NaCl, and LiCl aqueous solutions. According to our preceding study the XRD pattern of 0.5 M NaCl aqueous solution in this study was between those of water and 1.0 M NaCl aqueous solution, but near to 1.0 M NaCl aqueous solution.[39] For water first peak appeared at 18 nm^{-1}, at 20 nm^{-1} for NaCl and at 19 nm^{-1} for LiCl. Significant hydration formation in the CNTs caused the peaks position shift to higher angle and/or scattering parameter for aqueous solution system.[40] The peak around 45 nm^{-1} has been weakened while the second and third peaks at 30 and 52 nm^{-1} were newly appeared, even though for LiCl aqueous solution those peaks were rather weak. Those peaks were similar scattering parameters to the XRD peaks of CNTs. However, those peaks are presumed that ice-like cluster formation of water in 2 nm CNT,[41] this is because to remove those peaks more than 30% scattering intensity for NaCl electrolyte solution had to be depressed, further, despite difference in ion species those peaks for LiCl electrolyte solution were rarely observed, can be shown in Figure 3. Small Peaks appeared at 30 and 52 nm^{-1} for Li electrolyte solution because Li ions interacted with water by stronger hydration than Na ions, consequently hydrogen bonds between water were weakened. Thus, Ice-like cluster formation was prevented, and the peaks around 30 and 52 nm^{-1} disappeared.

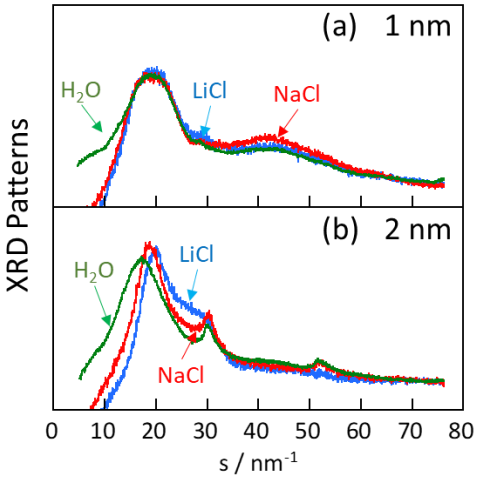

Figure 2. XRD patterns of Water (green), NaCl (red) and LiCl (blue) aqueous solutions in the CNTs with diameter 1 nm (a) and 2 nm (b).

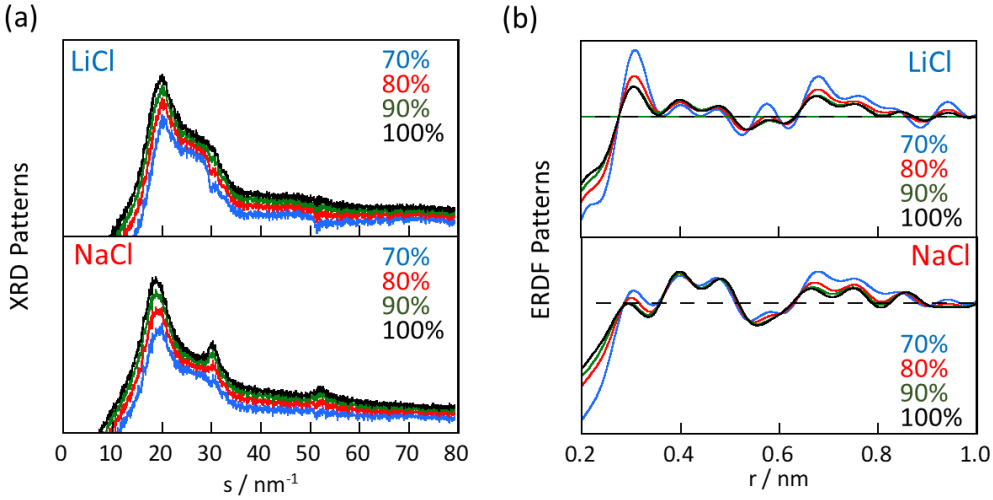

Figure 3 (a) Subtracted XRD patterns of electrolyte solutions using several scattering intensities for CNT. The XRD peak intensities were changed from 100% to 70% of the presumable intensities. (b) Electron radial distribution function calculated by Fourier

transformation of subtracted XRD patterns. The peak positions were rarely changed when the assumed adsorption amounts were considerably changed.

Fourier transformation was used to calculate the ERDFs of aqueous electrolyte solutions and water depicted in figure 4a from the XRD patterns in figure 2. In the 1 and 2 nm CNTs there were a pronounced structure differences among NaCl and LiCl aqueous solutions, and this indicated that a small number of ions in comparison with water influenced the whole water structure much in the pore of CNTs. The ERDF patterns of electrolyte solutions in 1 and 2 nm CNTs were apparently different; those peaks in 2 nm CNT were rather narrower than 1 nm CNT. However, those agreed with our preceding study where supercritical gas-like and ice-like structures were observed for water adsorbed in 1 and 2 nm CNTs.[39] In case of 1 nm CNT, the major peak position of water appeared in 0.32 nm which was longer than the nearest neighbour distance 0.30 nm in bulk. On top of this, for NaCl main peak positioned at 0.37 nm, while for LiCl it was at 0.44 nm. In comparison of water peak position the main peak of aqueous solutions was moved to longer distance, corresponding to the second and third neighbour distances. The first peak of water appeared at 0.27 nm and 0.29-0.3 nm for NaCl and LiCl aqueous solutions in the 2nm CNTs. This suggested water–water distance was elongated by ions, since water–water correlation is considering the major contributor for peak intensity.[41] In order to detailed analyses of electrolytes and water structures those main peaks were deconvoluted into the multiple peaks.

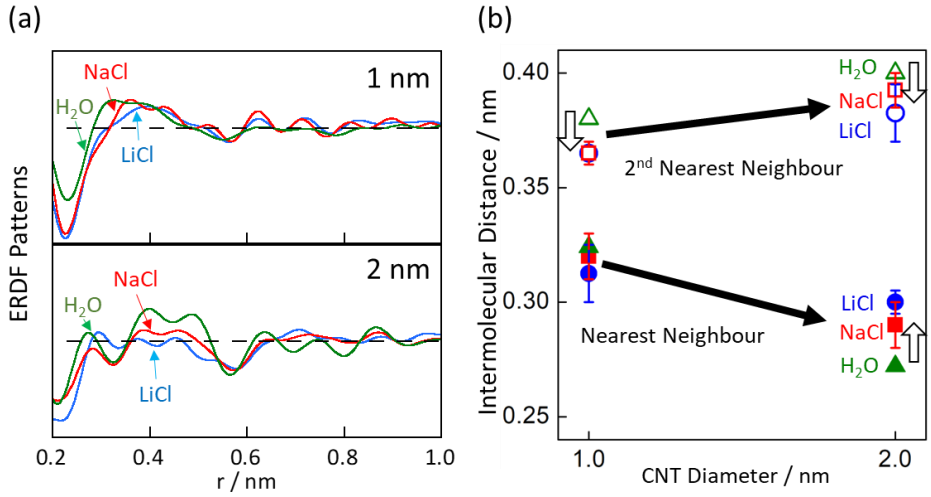

Figure 4 (a) ERDFs of NaCl and LiCl aqueous solutions and water in CNTs inside the 1 nm and 2 nm diameter CNTs. (b) The nearest- and second nearest-neighbour distances as a function of CNT diameter. Solid and open symbols represent the nearest and second neighbour distances, respectively. ●: LiCl, ■: NaCl, and ▲: water.

Figure 4b shows the definite change of the intermolecular distance as a function of CNT diameter. For water in 1 nm CNTs system, first nearest neighbouring water-water distance was at 0.32±0.00 nm and second nearest neighbouring water-water distance was at 0.38±0.00 nm. Whereas, the first nearest neighbour distances for NaCl and LiCl aqueous solutions inside the 1 nm CNT were 0.30 – 0.33 nm and the second nearest neighbour distances were 0.37±0.01 nm. The second nearest neighbour distances in water were thus longer than aqueous electrolyte. In the 2 nm CNTs, the first nearest neighbour distances were 0.27±0.00, 0.29±0.01, and 0.30±0.01 nm, for water and, NaCl and LiCl aqueous solutions respectively. The second nearest neighbour distances for water, NaCl and LiCl aqueous solutions were 0.40±0.00, 0.39±0.01 and 0.38±0.01 nm, respectively. The longest intermolecular distance of water was in 1 nm

CNT and shortest in the 2 nm CNT, while for aqueous solution those changes of shortened intermolecular distance with increasing CNT diameter were moderate. In these circumstances, the intermolecular distances of water and aqueous electrolyte were reversed in 1 and 2 nm CNTs. Those results suggested the transformation of water structures from supercritical gas-like structure to ice-like structure with changing CNT diameter from 1 to 2 nm, as mentioned above, whereas due to the formation of hydration between ion and water the structure transformations of aqueous solutions were obscure. Furthermore, due to the formation of hydration shell in both CNTs the second nearest neighbour distances in aqueous electrolyte were shorter than water, although structure difference between bulk water and aqueous solution was unobserved.[41]

MD simulations were performed in order to clarify the mechanism. The simulated snapshots of water, LiCl and NaCl electrolyte solutions systems after the accumulation for 2 ns in the simulations were illustrated in figure 5, 6 and 7. Water was fully adsorbed in those CNTs, however, it was hard to adsorb Li^+ in the smaller than 2.1 nm CNTs while for Na^+ it was smaller than 1.8 nm, although the ionic size of the Li^+ and Na^+ ions were smaller than the effective diameter of CNTs. one of the preceding work also reported this phenomenon.[3] This indicated that, ions were prevented from entering ion CNTs by the formation of rigid hydration structure. However, ion permeability was increased when the concentration was increased, this is because in case of higher concentration the probability of entering of ions inside the pore was raised as illustrated in Figure 7. According to the experimental XRD patterns, it was different for bare CNTs, aqueous solutions adsorbed CNTs and water adsorbed CNTs,

therefore we assumed that all kind of ions can be entered inside the CNT pores. The calculation time for the simulation was few nano-seconds which very small compare to the experimental time about a week was, this time limitation provided the disagreement between simulations and experiments. However, the outputs of MD simulations were used to clarify the molecular level confined structures.

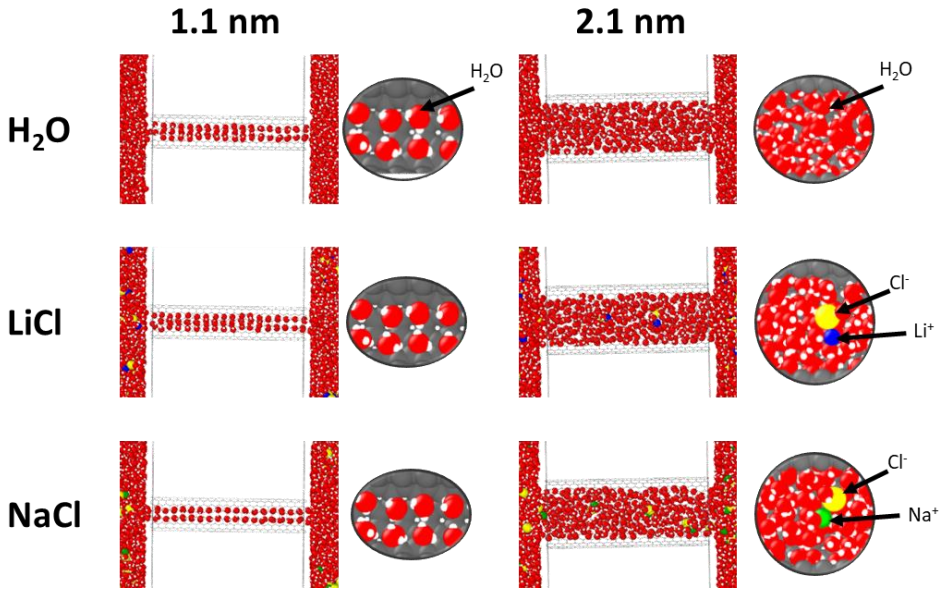

Figure 5. Snapshots of LiCl and NaCl aqueous solutions, and water adsorbed in CNTs.

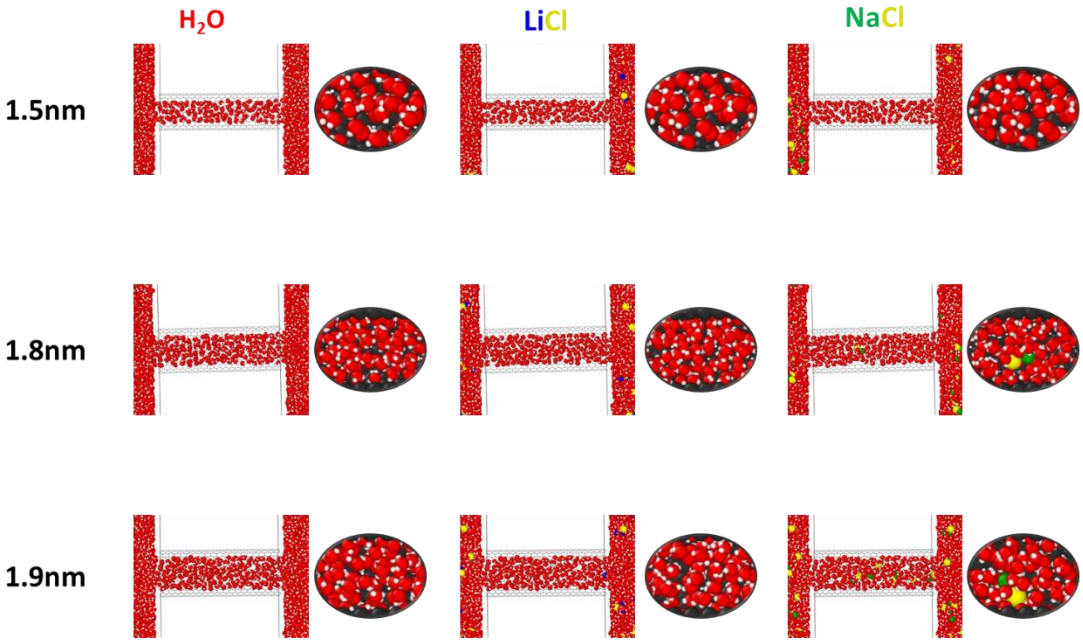

Figure 6. Simulation snapshot of LiCl and NaCl after 2 ns in the different pores. Li^+, Na^+, Cl^- and water were depicted as blue, green, yellow and red colours, respectively.

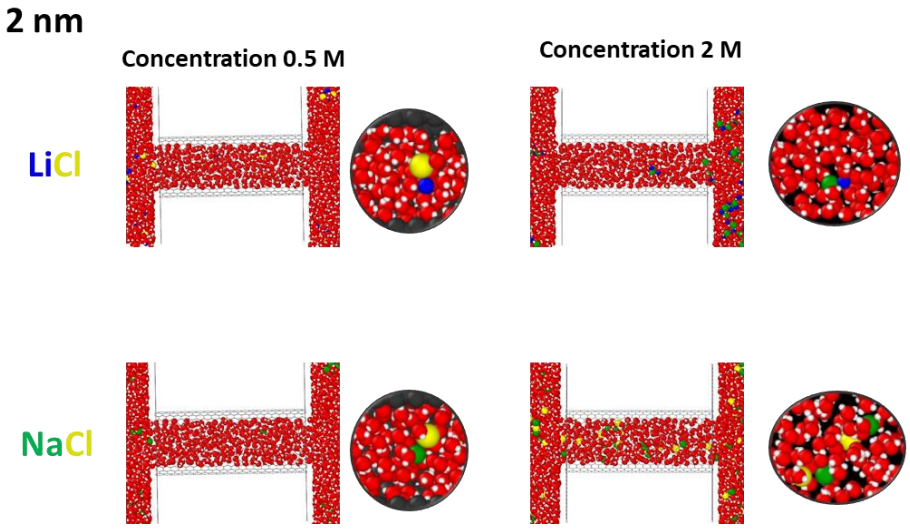

Figure 7. Simulation snapshot of LiCl and NaCl after 2 ns in the 2 nm pores at concentration 0.5 M and 2 M. Li^+, Na^+, Cl^- and water were depicted as blue, green, yellow and red colours, respectively.

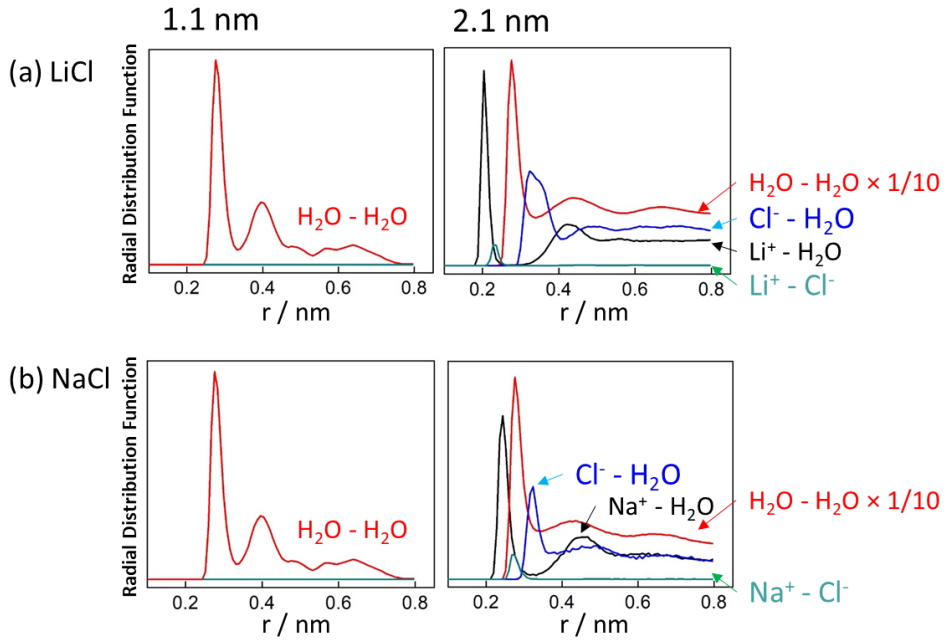

Figure 8. Simulated radial distribution functions of LiCl (a) and NaCl aqueous solutions (b) in CNTs.

The radial distribution functions (RDFs) calculated form the MD simulation for aqueous electrolytes and water were depicted in the figure 9 and 10. All of the systems were dominated by water-water correlations, even though in the calculations atomic scattering functions were added. For all the systems considered, the nearest neighbouring water-water distances were 0.28 nm, while by formation of hydrogen bonds the second neighbouring peaks were appeared approximately at 0.40–0.44 nm. On the other hand, bulk water 0.30 nm was the first nearest neighbour and 0.46 nm was the second-nearest neighbour distances. This value was similar to the ERDF calculated form the experiments in 2 nm CNT, however in case of 1 nm CNT, experimental value longer than this. The shorter nearest neighbour distances in the MD simulations than the experiments suggested that water was rather slender in the 1 nm CNT system with water. In 1 nm CNT, in aqueous electrolytes system the ion–water correlation influenced the

nearest neighbour distance, even though those distances were retrained far from the water intermolecular distance calculated from the MD simulation. In case of 2 nm CNTs, the further nearest neighbour distance of electrolyte solutions rather than water mainly facilitated by the Cl^- ion and water correlation, since according to the simulations the Cl^-–water distance was 0.32 nm and water–water distances was 0.28 nm. The nearest neighbour distance calculated from the experiments, for water was 0.27±0.01 nm and for the electrolytes 0.29–0.30 nm. Thus, ions were contributed by forming strong hydration shell instead of the formation of hydrogen bonds to connecting water in 1 nm CNTs and scatter the water in 2 nm CNT. Likewise, figure 10 depicted the RDFs of LiCl and NaCl aqueous electrolytes with 0.5 and 2.0 M concentrations indicated the similar structures. The hydration numbers calculated from MD simulations proposed that with the decreasing of the CNT diameter than 1.8 nm the hydration number of Na^+ were significantly decrease; the hydration number in 1.8 nm CNT was 4.2, which was 5.0 in 2.1 nm CNT, while it was 5.8 in the bulk. Besides, in case of Li^+ the hydration number in 2.1 nm CNT was 3.2 and, in the bulk, it was 3.8; while those of Cl^- ions was 6.3 in 2.1 nm CNT and 5.2 was in bulk. These phenomena indicated the formation of strong hydration shell, although little bit decreasing of the hydration number can be seen. Owing to the stronger Li^+-water interaction than the Na^+–water Li^+ showed more bulk like hydration number in 2 nm CNT compared to Na^+. Likewise experimental differential XRD patterns in simulations the water structure confined in CNTs have been extensively influenced by the Li^+.

(a) LiCl

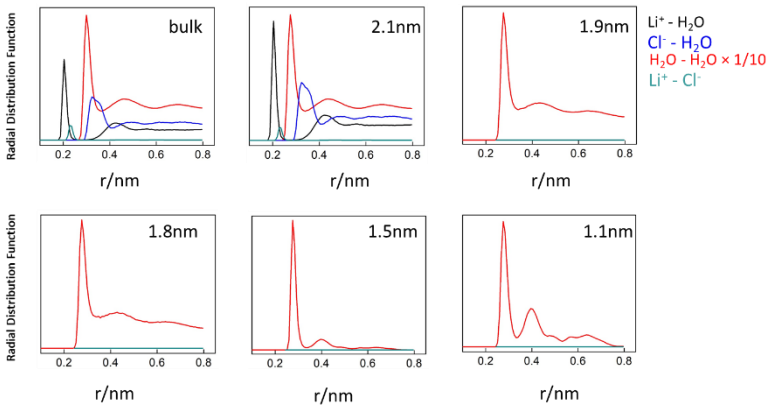

(b) NaCl

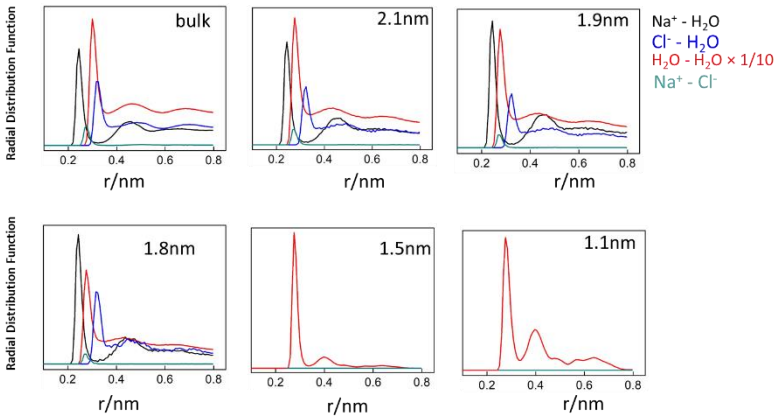

(c) Water

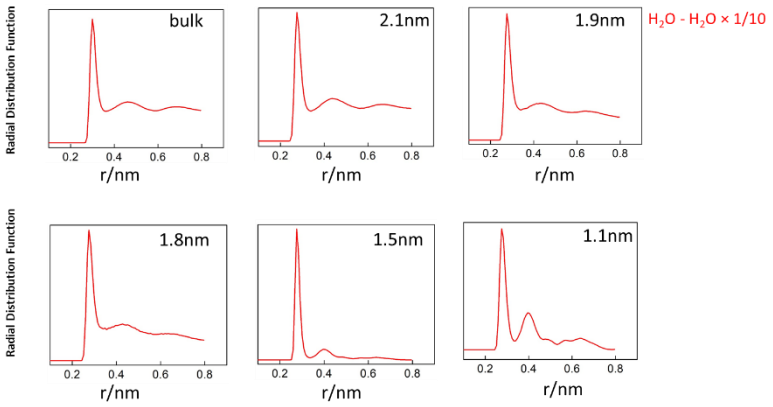

Figure 9 Simulated radial distribution functions of LiCl (a) and NaCl aqueous solutions (b) and water (c) in CNTs and bulk.

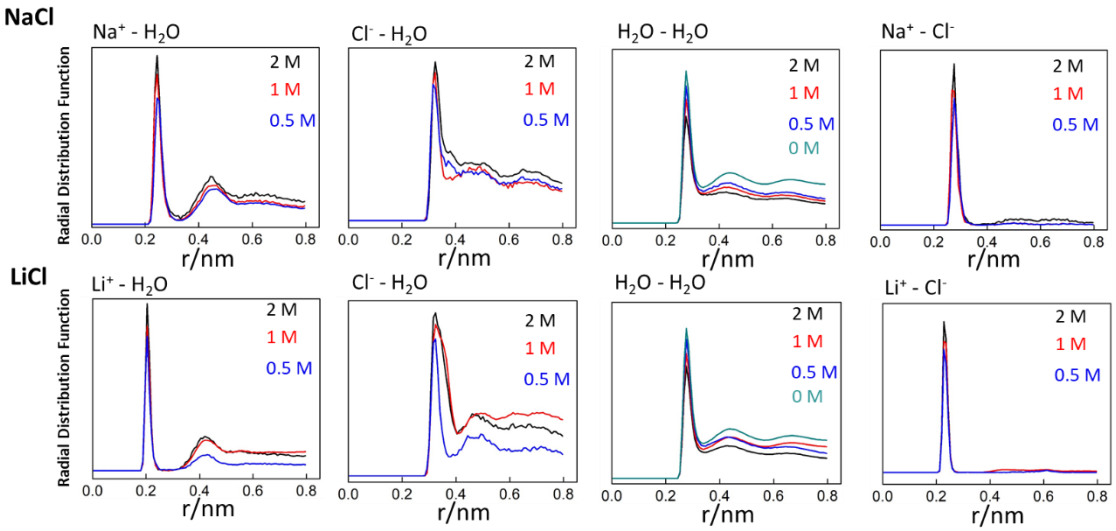

Figure 10. Simulated radial distribution functions of NaCl and LiCl aqueous solutions in the 2 nm pores with concentration 2 M (black), 1 M (red), 0.5 M (blue), and 0 M (cyan)

4.4 Conclusion

In this chapter of the theses, we employed both XRD experiments and MD simulations to evaluate the cylindrical nanopore CNT confined structure of NaCl and LiCl electrolyte solution as well as the water. In case of water, the intermolecular distance for water was 0.32 nm in 1 nm CNTs while 0.27±0.01 in 2 nm CNTs, while the distance for bulk ice was 0.28 nm and 0.30 nm for liquid. These valued demonstrated that in the 1 nm CNTs water molecules are more dispersed than bulk liquid water while in the 2 nm CNTs was closer, suggesting that the water formed supercritical gas structure in 1 nm CNTs while ice-like structure in 2 nm CNTs. The intermolecular distances become like bulk liquid water for aqueous electrolytes. This phenomenon clearly indicated the influence of ions in the change of intermolecular distances. The ions separated water molecules in 2 nm CNT while slightly connected the water molecules in 1 nm CNTs by forming strong hydration shell instead of hydrogen bonds. In addition, Na^+ shows significant dehydration while changing the CNTs diameters form 2 nm, whereas Li^+ construct strong hydration shell rather than Na^+ in 2 nm CNTs. Therefore, the change of the intermolecular distances of aqueous electrolytes inside the CNTs not only influenced by the confinement effect but also by the correlation between ion-ion and ion-water.

References:

1. Zhang, L. L.; Zhao, X. S., Carbon-Based Materials as Supercapacitor Electrodes. *Chemical Society Reviews* **2009**, *38*, 2520-2531.

2. Chmiola, J.; Yushin, G.; Gogotsi, Y.; Portet, C.; Simon, P.; Taberna, P. L., Anomalous Increase in Carbon Capacitance at Pore Sizes Less Than 1 Nanometer. *Science* **2006**, *313*, 1760-1763.

3. Feng, G.; Qiao, R.; Huang, J.; Sumpter, B. G.; Meunier, V., Atomistic Insight on the Charging Energetics in Subnanometer Pore Supercapacitors. *The Journal of Physical Chemistry C* **2010**, *114*, 18012-18016.

4. Kajdos, A.; Kvit, A.; Jones, F.; Jagiello, J.; Yushin, G., Tailoring the Pore Alignment for Rapid Ion Transport in Microporous Carbons. *Journal of the American Chemical Society* **2010**, *132*, 3252-3253.

5. Kondrat, S.; Pérez, C. R.; Presser, V.; Gogotsi, Y.; Kornyshev, A. A., Effect of Pore Size and Its Dispersity on the Energy Storage in Nanoporous Supercapacitors. *Energy & Environmental Science* **2012**, *5*, 6474-6479.

6. Yu, M.; Lin, D.; Feng, H.; Zeng, Y.; Tong, Y.; Lu, X., Boosting the Energy Density of Carbon Aqueous Supercapacitors by Optimizing the Surface Charge. *Angew. Chem.* **2017**, *56*, 5454-5459

7. Endo, M.; Maeda, T.; Takeda, T.; Kim, Y. J.; Koshiba, K.; Hara, H.; Dresselhaus, M. S., Capacitance and Pore-Size Distribution in Aqueous and Nonaqueous Electrolytes Using Various Activated Carbon Electrodes. *J. Electrochem. Soc.* **2001**, *148*, 910-914

8. Qu, D.; Shi, H., Studies of Activated Carbons Used in Double-Layer Capacitors. *J. Power Sources.* **1998**, *74*, 99-107.

9. Barbieri, O.; Hahn, M.; Herzog, A.; Kotz, R., Capacitance Limits of High Surface Area Activated Carbons for Double Layer Capacitors. *Carbon* **2005**, *43*, 1303-1310

10. Kierzek, K.; Frackowiak, E.; Lota, G.; Gryglewicz, G.; Machnikowski, J., Electrochemical Capacitors Based on Highly Porous Carbons Prepared by Koh Activation. *Electrochem. Acta.* **2004**, *49*, 515-523

11. Shiraishi, S.; Kurihara, H.; Okabe, K.; Hulicova, D.; Oya, A., Electric Double Layer Capacitance of Highly Pure Single-Walled Carbon Nanotubes (Hipcotm Buckytubestm) in Propylene Carbonate Electrolytes. *Electrochem. Commun.* **2002**, *4*, 593-598

12. Barisci, J. N.; Wallace, G. G.; Baughman, R. H., Electrochemical Characterization of Single-Walled Carbon Nanotube Electrodes. *J. Electrochem. Soc.* **2000**, *147*, 4580-4583.

13. Portet, C.; Yang, Z.; Korenblit, Y.; Gogotsi, Y.; Mokaya, R.; Yushin, G., Electrical Double-Layer Capacitance of Zeolite-Templated Carbon in Organic Electrolyte. *Journal of The Electrochemical Society* **2009**, *156*, A1-A6.

14. Morishita, T.; Soneda, Y.; Tsumura, T.; Inagaki, M., Preparation of Porous Carbons from Thermoplastic Precursors and Their Performance for Electric Double Layer Capacitors. *Carbon* **2006**, *12* 2360-2367.

15. Morishita, T.; Tsumura, T.; Toyoda, M.; Przepiorski, J.; Morawski, A. W.; Konno, H.; Inagaki, M., A Review of the Control of Pore Structure in Mgo-Templated Nanoporous Carbons. *Carbon* **2010**, *10*, 2690-2707.

16. Xu, B.; Wu, F.; Chen, R.; Cao, G.; Chen, S.; Zhou, Z.; Yang, Y., Highly Mesoporous and High Surface Area Carbon: A High Capacitance Electrode Material for Edlcs with Various Electrolytes. *Electrochem. Commun.* **2008**, *10*, 795-797

17. Simon, P.; Gogotsi, Y., Materials for Electrochemical Capacitors. *Nature Materials* **2008**, *7*, 845.

18. Zahi, Y.; Dou, Y.; Zhao, D.; Fulvio, P. F.; Mayes, R. T.; Dai, S., Carbon Materials for Chemical Capacitive Energy Storage. *Adv. Mater.* **2011**, *23*, 4828-4850

19. Inagaki, M.; Konno, H.; Tanaike, O., Carbon Materials for Electrochemical Capacitors. *J. Power Sources.* **2010**, *24*, 7880-79036.

20. Sansom, M. S. P.; Biggin, P. C., Water at the Nanoscale. *Nature* **2001**, *414*, 157-159.

21. Ohkubo, T.; Takehara, Y.; Kuroda, Y., Water-Initiated Ordering around a Copper Ion of Copper Acetate Confined in Slit-Shaped Carbon Micropores. *Microporous Mesoporous Mater.* **2012**, *154*, 82-86

22. Nishi, M.; Ohkubo, T.; Urita, K.; Moriguchi, I.; Kuroda, Y., Experimental Information on the Adsorbed Phase of Water Formed in the Inner Pore of Single-Walled Carbon Nanotube Itself. *Langmuir* **2016**, *32*, 1058-1064.

23. Feng, G.; Cummings, P. T., Supercapacitor Capacitance Exhibits Oscillatory Behavior as a Function of Nanopore Size. *The Journal of Physical Chemistry Letters* **2011**, *2*, 2859-2864.

24. Shao, Q.; Huang, L.; Zhou, J.; Lu, L.; Zhang, L.; Lu, X.; Jiang, S.; Gubbins, K. E.; Shen, W., Molecular Simulation Study of Temperature Effect on Ionic Hydration in Carbon Nanotubes. *Physical Chemistry Chemical Physics* **2008**, *10*, 1896-1906.

25. Shao, Q.; Zhou, J.; Lu, L.; Lu, X.; Zhu, Y.; Jiang, S., Anomalous Hydration Shell Order of Na+ and K+ inside Carbon Nanotubes. *Nano Letters* **2009**, *9*, 989-994.

26. Ohba, T., Anomalously Enhanced Hydration of Aqueous Electrolyte Solution in Hydrophobic Carbon Nanotubes to Maintain Stability. *ChemPhysChem* **2014**, *15*, 415-419

27. Oya, Y.; Hata, K.; Ohba, T., Interruption of Hydrogen Bonding Networks of Water in Carbon Nanotubes Due to Strong Hydration Shell Formation. *Langmuir* **2017**, *33*, 11120-11125.

28. Fu, J.; Liu, Y.; Wu, J., Molecular Density Function Theory for Multiscale Modelling of Hydration Free Energy. *Chem Eng Sci.* **2015**, *126*, 370-382.

29. Hu, H.; Yang, W., Free Energies of Chemical Reactions in Solution and in Enzymes with Ab Initio Quantum Mechanics/Molecular Mechanics Methods. *Annual Review of Physical Chemistry* **2008**, *59*, 573-601.

30. Li, G.; Zhang, X.; Cui, Q., Free Energy Perturbation Calculations with Combined Qm/Mm Potentials Complications, Simplifications, and Applications to Redox Potential Calculations. *The Journal of Physical Chemistry B* **2003**, *107*, 8643-8653.

31. Schwarz, K. A.; Sundararaman, R.; Letchworth-Weaver, K.; Arias, T. A.; Hennig, R. G., Framework for Solvation in Quantum Monte Carlo. *Physical Review B* **2012**, *85*, 201102.

32. Sundararaman, R.; Letchworth-Weaver, K.; Arias, T. A., A Computationally Efficacious Free-Energy Functional for Studies of Inhomogeneous Liquid Water. *J. Chem. Phys.* **2012**, *137*, 044107-044112

33. Maiti, A., Multiscale Moldeling with Carbon Nanotubes. *Microelectron J.* **2008**, *39*, 208-221

34. Martinez, L.; Andrade, R.; Birgin, E. G.; Martinez, J. M., A Package for Building Initial Configurations for Molecular Dynamics Simulations. *J. Comput. Chem.* **2009**, *30*, 2157-2164

35. Martinez, J. M.; Martinez, L., Packing Optimization for Automated Generation of Complex System`S Initial Configurations for Molecular Dynamics and Docking. *J. Comput. Chem.* **2003**, *24*, 819-825

36. Ohba, T.; Takase, A.; Ohyama, Y.; H., K., Grand Canonical Monte Carlo Simulations of Nitrogen Adsorption on Graphene Materials with Varying Layer Number. *Carbon* **2013**, *61*, 40-46

37. Jorgensen, W. L.; Chandrasekhar, J.; Madura, J. D.; Impey, R. W.; Klein, M. L., Comparison of Simple Potential Functions for Simulating Liquid Water. *The Journal of Chemical Physics* **1983**, *79*, 926-935.

38. Ryckaert, J.; Ciccotti, G.; Berendsen, H. J. C., Numerical Integration of the Certesian Equations of Motion of a System with Constrains: Molecular Dynamics of N-Alkanes. *J. of Comp. Phys.* **1977**, *23*, 327-341

39. Ohba, T., Size-Dependent Water Structures in Carbon Nanotubes. *Angew. Chem. Int. Ed.* **2014**, *53*, 8032-8036.

40. Ohba, T.; Taira, S.-i.; Hata, K.; Kaneko, K.; Kanoh, H., Predominant Nanoice Growth in Single-Walled Carbon Nanotubes by Water-Vapor Loading. *RSC Advances* **2012**, *2*, 3634-3637.

41. Ohba, T.; Hata, K.; Kanoh, H., Significant Hydration Shell Formation Instead of Hydrogen Bonds in Nanoconfined Aqueous Electrolyte Solutions. *Journal of the American Chemical Society* **2012**, *134*, 17850-17853.

Chapter 5

Conclusions

In order of decrease the concentration of the CO_2 in the atmosphere improvement of the technology for CO_2 capture and removal as well as improvement of the alternative renewable energy technology is highly essential. The presence of nitrogen atoms in the structure can essentially influence the CO_2 uptake amount. One of my study I have focused to find out the mechanism how the doping of hetero atoms like nitrogen can affect the CO_2 adsorption and sensing performance. On the other hand, aqueous electrolytes show unique structure in the nanopores and this structural change highly influence the performance of the system. In this part of my study I tried to resolve the structure of the aqueous electrolytes in cylindrical nanopore of CNTs.

The conclusions related with the improvement of CO_2 uptake technology and renewable energy in the respective chapters are summarized as follows:

Chapter 3: High CO_2 Sensitivity and Reversibility on Nitrogen-Containing Polymer by Remarkable CO_2 Adsorption on Nitrogen Sites

In this chapter, comprehensive study of simulation and experiments demonstrated, how the presence of the nitrogen atoms in a polymer structure can essentially influence the CO_2 adsorption and sensing properties. The presence of the N atoms in the polymer structure significantly change the partial charge distribution throughout the structure and nitrogen sites possess high negative partial charge, whereas the polymer without nitrogen atoms shows neutral partial charge distribution. Highly electronegative nitrogen sites mainly attract the electropositive carbon atom of CO_2. At different

temperature such as 243, 273 and 303 K polymer with nitrogen atoms shows relatively higher CO_2 adsorption amount rather than polymer without nitrogen atoms. The self-diffusion coefficient calculated form the MD simulations suggested that, the diffusion of the CO_2 mostly restricted by the nitrogen sites even at higher temperature rather than other ring and vinyl sites. Nitrogen sites of the polymer can act as a Lewis base as CO_2 considered as Lewis acid and demonstrated high sensing performance. Thus, doping of nitrogen atoms in the structure can remarkable improve the CO_2 adsorption capability and sensing performance.

Chapter 4: Anomalous Changes of Intermolecular Distance in Aqueous Electrolytes in Narrow Pores of Carbon Nanotubes

In this chapter, by using XRD analysis and MD simulations the structure of water, NaCl and LiCl electrolyte solutions have been evaluated in the pores of CNTs. In case of water, the value of intermolecular distances in 1 nm CNTs (0.32 nm) and 2 nm CNTs (0.27±0.01 nm) suggested that the phase of water has been change due to the change of the diameter of the nanopores. In 1 nm CNT water was far more separated than bulk water which is considered as supercritical gas phase and ice like structure formed in the 2 nm CNT. Intermolecular distances calculated for aqueous electrolyte in CNTs suggested bulk like liquid water, which indicated that the ions play a vital rule to change the structure in both 1 nm and 2 nm CNTs by forming hydration shell. Moreover, Na^+ were desolvated with the decrease of the CNT diameter from 2 nm, while Li^+ formed relatively strong hydration shell. Therefore, the change of the intermolecular distance in the nanopores of CNTs not only influenced by the confinement effect but also effected by the correlation between ion-water and ion-ion interactions.

Acknowledgements

During the three years, I have had a great pleasure of working. All the work in this thesis would not be completed without the helps from numerous people who I want to take the opportunity to thank them here. First and foremost, I would like to thank my supervisor Professor Dr. Tomonori Ohba for his patient support, training and kindness. He has given me the courage to delve into the research.

My gratitude also goes out to my friend and laboratory mate Ms. Sharifa Faraezi for her continues support and useful discussion throughout the course of this thesis. I am grateful to the Mr. Daiki Hoshi who made my life easier in Japan and helped me continuously. I am also thankful to Mr. Takumi Watanabe for his technical advice on adsorption measurement. I would like to thank all the other co-authors who somewhat contributed to all my researches.

I would like to thank the Supercomputer Center, the Institute for Solid State Physics, the University of Tokyo for the use of the facilities to conduct the simulations of this thesis. I am also grateful to the JGC-S scholarship foundation a and JASSO for their financial support.

Finally, I would never have made it without my family. I would like to thank my mother who has always been there for me, my father for his love and a great support until the end of his life and my sisters and bothers for their loves and cares.

July 2019

MD SHARIF KHAN